J. Fluid Mech. (2010), *vol.* 653, *pp.* 175–219.
doi:10.1017/S0022112010000200

Velocity distribution function and correlations in a granular Poiseuille flow

MEHEBOOB ALAM† AND V. K. CHIKKADI

Engineering Mechanics Unit, Jawaharlal Nehru Centre for Advanced Scientific Research, Jakkur P.O., Bengaluru 560064, Karnataka, India

(Received 28 March 2009; revised 11 January 2010; accepted 11 January 2010; first published online 6 May 2010)

Probability distribution functions of fluctuation velocities ($P(u_x)$ and $P(u_y)$, where u_x and u_y are the fluctuation velocities in the x- and y-directions, respectively; the gravity is acting along the periodic x-direction and the flow is bounded by two walls parallel to the y-direction) and the density and the spatial velocity correlations are studied using event-driven simulations for an inelastic smooth hard disk system undergoing gravity-driven granular Poiseuille flow (GPF). It is shown that for GPF with smooth and/or perfectly rough walls the Maxwellian/Gaussian is the leading-order distribution over a wide range of densities in the quasi-elastic limit, which is a surprising result, especially for a dilute granular gas for which the Knudsen number belongs to the transitional flow regime. The signature of wall-roughness-induced dissipation mainly shows up in the $P(u_x)$ distribution in the form of a sharp peak for negative velocities in the near-wall region. Both $P(u_x)$ and $P(u_y)$ distributions become asymmetric with increasing dissipation at any density, and the emergence of density waves, which appear in the form of sinuous wave/slug at low-to-moderate values of mean density, makes these asymmetries stronger, especially in the presence of a slug. At high densities, the flow degenerates into a dense plug (where the density approaches its maximum limit and the shear rate is negligibly small) around the channel centreline and two shear layers (where the shear rate is high and the density is low) near the walls. The distribution functions within the shear layer follow the characteristics of those at moderate mean densities. Within the dense plug, the high-velocity tails of both $P(u_x)$ and $P(u_y)$ appear to undergo a transition from Gaussian in the quasi-elastic limit to power-law distributions at large inelasticity of particle collisions. For dense flows, it is shown that although the density correlations play a significant role in enhancing the velocity correlations when the collisions are sufficiently inelastic, they do not induce velocity correlations when the collisions are quasi-elastic for which the distribution functions are close to Gaussian. The combined effect of enhanced density and velocity correlations around the channel centreline with increasing inelastic dissipation seems to be responsible for the emergence of non-Gaussian high-velocity tails of distribution functions.

1. Introduction

Highly excited granular materials, generally referred to as rapid granular flows or granular gases, resemble molecular fluids as the interactions are binary and instantaneous (Campbell 1990; Goldhirsch 2003). These similarities have been

† Email address for correspondence: meheboob@jncasr.ac.in

exploited in formulating the theory of rapid granular flows, which is largely based on the dense gas kinetic theory that incorporates the 'inelastic' nature of particle collisions (Haff 1983; Jenkins & Savage 1983; Lun 1991; Sela & Goldhirsch 1998; Brey, Dufty & Santos 1999; Garzo & Dufty 1999; Alam *et al.* 2002; Mitarai, Hayakawa & Nakanishi 2002; Brilliantov & Pöschel 2004; Tij & Santos 2004; Kumaran 2006). At the heart of such gas- or liquid-state continuum theories, there lies the concept of 'coarse-graining' over single-particle distribution functions while making a transition from the particle-level properties to the macro-scale/hydrodynamic fields. The Maxwell–Boltzmann (Gaussian/Maxwellian) distribution plays the role of the 'equilibrium' distribution function for molecular gases at thermodynamic equilibrium. In contrast, however, due to the inherent microscopic dissipation of particle collisions, the granular gas does not have an 'equilibrium' uniform state.

However, there are 'non-equilibrium' (driven) steady states for various canonical granular flow configurations (e.g. simple shear flow) for which the Maxwellian distribution is the leading-order velocity distribution (Sela & Goldhirsch 1998) in the double limit of both Knudsen number and inelasticity approaching zero. A related issue is the continuum boundary conditions for granular flows (Hui *et al.* 1984; Jenkins & Richman 1986). While deriving boundary conditions using dense-gas kinetic theory formalism, it is often assumed that the distribution function in the near wall region is the same as that in the bulk – this assumption is unlikely to hold. It is clear that a systematic study of both the 'bulk' and 'wall' distribution functions is of fundamental interest from the viewpoint of developing constitutive models and boundary conditions for granular flows. Simulations and experiments on the above would help to pinpoint the range of validity of any adopted constitutive theory and boundary conditions.

In 'driven' granular gases, the deviation of velocity distribution from a Gaussian has been studied through theory (Esipov & Pöschel 1997; van Noije & Ernst 1998; Sela & Goldhirsch 1998), simulation (Taguchi & Takayasu 1995; Goldhirsch & Tan 1996; Puglisi *et al.* 1998; Cafiero, Luding & Herrmann 2000; Montanero & Santos 2000; Moon, Shattuck & Swift 2001; van Zon & MacKintosh 2004; Gayen & Alam 2008) and experiment (Natarajan, Hunt & Taylor 1995; Losert *et al.* 1999; Rouyer & Menon 2000; Blair & Kudrolli 2001; Baxter & Olafsen 2003; Moka & Nott 2005). Esipov & Pöschel (1997) have solved the Boltzmann equation for inelastic hard spheres at large velocities. For the freely evolving system, they found a spatially homogeneous distribution function for which the large velocities decay as $f \sim \exp(-\beta v/v_0(t))$, where $v_0(t)$ is the time-dependent thermal velocity and $\beta \sim 1/\epsilon$ is a constant, related to the inelasticity $\epsilon = 1 - e_n^2$, defined in terms of the coefficient of normal restitution e_n. For a rapid flow of smooth, inelastic spheres, Sela & Goldhirsch (1998) solved the Boltzmann equation perturbatively upto third order by performing a double expansion of velocity distribution in Knudsen number (Kn) and the degree of inelasticity (ϵ). The single-particle velocity distributions for homogeneous granular fluids of inelastic hard spheres were studied, based on the Enskog–Boltzmann equation for the unforced and heated case, by van Noije & Ernst (1998). They showed that velocity distribution in the heated steady state exhibits a high-energy tail $\sim\exp(-\beta c^{3/2})$, where c is the velocity scaled by the thermal velocity and $\beta \sim 1/O(\epsilon)$ with ϵ being the degree of inelasticity.

Montanero & Santos (2000) investigated distribution functions in a heated granular gas using the direct simulation Monte Carlo method, and their results on high-velocity tails agree with the prediction of van Noije & Ernst (1998); they also showed that the distribution functions depend on the type of heating. That the high

tails are consistent with $\sim\exp(-\beta c^{3/2})$ for $e_n < 0.5$ has been shown by Moon *et al.* (2001), who investigated the steady-state velocity distributions in three dimensions using molecular dynamics simulations for a homogeneously heated granular gas. A simulation of quasi-two-dimensional granular gas (with spheres restricted to move in a plane) subject to multiplicative driving proportional to $|v(x)|^{\delta}$ of the local particle velocity $v(x)$ was performed by Cafiero *et al.* (2000); here δ can take positive or negative values with $\delta = 0$ being the case of homogeneous driving. For $\delta = 1$, the tails of the velocity distributions were found to follow a stretched exponential, $f(v_x) \sim \exp(-\beta|v_x - \langle v_x \rangle|^{\alpha})$, with the exponent α varying between 0.5 and 2 as a function of restitution coefficient e_n. They further showed that the non-Gaussianity is restricted to high-velocity tails for large e_n; however, the whole range of velocities is affected by non-Gaussianity for small e_n when $\delta = 1$; for negative values of $\delta = -0.25$ and -0.5, they found that the distribution function remains close to a Gaussian even at much smaller values of e_n. It has been shown (Taguchi & Takayasu 1995) that the velocity fluctuations in a vibrated bed of powder follow a Gaussian distribution in the solid phase and a non-Gaussian distribution in the fluidized phase. These authors considered the effect of clustering by inelastic collisions and showed that the non-Gaussian distribution in the fluidized phase is well approximated by a t-distribution with a power law of exponent -3. From simulations of the plane shear flow (Goldhirsch & Tan 1996), it has been shown that the velocity distribution function can be fitted by an exponent of a second-order polynomial in the norm of the fluctuating velocities with angle-dependent coefficients.

More recently, the non-Gaussian velocity distributions have been studied by van Zon & MacKintosh (2004) for a dilute granular gas, but they did not find any universal velocity distribution of the form $P(v) \sim \exp\left(-\beta v^{1.5}\right)$. Interestingly, e_n and q, where e_n is the coefficient of normal restitution and q is the ratio of the number of heating events to the number of particle–particle collisions, are the only parameters that control the characteristics of velocity distributions: distributions are Gaussian for $q \gg 1$ and become strongly non-Gaussian for $q \ll 1$. Considering a simple model of a two-dimensional inelastic gas without spatial degrees of freedom, they showed that the results obtained from this model qualitatively matched with their simulation results, implying that the non-Gaussianity is not a consequence of spatial correlations. It is rather the cascade of energy from high-energy particles to slow-moving particles that decides the behaviour of the velocity distribution.

Granular materials confined between two vertical plates and driven into a steady state via vertical vibrations were recently studied experimentally by Rouyer & Menon (2000). They observed a characteristic velocity distribution of the form $P(v) \sim \exp(-\beta v^{\alpha})$, with $\alpha = 1.55 \pm 0.1$, occurring over a wide range of frequency and amplitude of vibrations which also covers from the dilute-to-dense systems. This result is in tune with earlier experiments on a vertically vibrated granular system (Losert *et al.* 1999) at higher excitations for which the particle–particle collisions were comparable with the particle–plate collisions (i.e. $Kn = O(1)$). Losert *et al.* (1999) also showed that the distribution function approaches an exponential for $Kn \ll 1$. The 3/2-exponent of the high-energy tails of the velocity distribution function is in tune with the theoretical result (van Noije & Ernst 1998). In contrast, however, some later experiments (Blair & Kudrolli 2001; Baxter & Olafsen 2003) showed that the high-velocity tails cannot be described by a stretched exponential with a 'single' universal exponent.

It is clear from the above discussion that a variety of velocity distributions can occur in granular flows: Gaussian, power law, exponential and stretched exponential.

The reasons for the observed deviation from a Gaussian are also varied, e.g. inelastic dissipation (Taguchi & Takayasu 1995; Losert *et al.* 1999), velocity correlations (Blair & Kudrolli 2001), spatial correlation (Puglisi *et al.* 1998), heating type (Montanero & Santos 2000), energy cascading (van Zon & MacKintosh 2004) and velocity and orientational correlations (Gayen & Alam 2008). Despite a host of research works, there is a lack of consensus on why the distribution functions are non-Gaussian in a driven granular gas. A specific form of distributions could be very specific to a given flow or for a given flow regime or for a given flow condition. Therefore, a case-by-case study of velocity distribution functions for different flow configurations is needed.

In this paper we present event-driven simulation results on the velocity distribution functions and the density and spatial velocity correlations in a gravity-driven Poiseuille flow of inelastic smooth hard disks. Our focus is (i) to probe the distribution functions in the quasi-elastic limit over a range of densities encompassing the Boltzmann limit and the ultra-dense flows near the close-packing limit, as well as to probe the crucial role of wall roughness on distribution functions; (ii) to characterize and quantify their deviations, if any, from a Maxwellian with increasing dissipation as well as at different 'local' hydrodynamic conditions in terms of the kurtosis and skewness of distributions; (iii) to characterize the role of density waves on distribution functions; and (iv) to pinpoint the role of density and spatial velocity correlations on the observed non-Gaussianity. Some preliminary results on the velocity distributions in GPF for low-to-moderate densities have been published by us (Vijayakumar & Alam 2007), and the present effort is a detailed characterization of distribution functions and correlations for low-to-very-dense systems with interesting new results.

2. Simulation method

Even though the 'inelastic' hard-sphere model is the simplest model for granular materials, it has been used successfully to emulate many interesting features in the rapid flow regime (Campbell 1990; Herrmann & Luding 1998; Goldhirsch 2003; Aranson & Tsimring 2006), which is the focus of our study. The collision model and the simulation method are the same as in our previous work (Vijayakumar & Alam 2007), and below we briefly recall some of their salient features for the sake of completeness.

2.1. *Granular Poiseuille flow and inelastic hard-disk model*

A sketch of the simulated system is shown in figure 1, which is a channel of length L along the periodic x-direction and bounded by two plane solid walls, parallel to the x-direction, with a separation of width W (along the y-direction). Within the channel, we randomly put a collection of N identical smooth, rigid, inelastic disks of unit mass and diameter d, and the disks are assigned random velocities. With this initial configuration, the material is allowed to flow along the x-direction (driven by gravitational acceleration, g).

The interactions that are allowed are instantaneous 'dissipative' collisions between pairs of particles and between a particle and the walls. The dissipative nature of particle collisions is characterized by the coefficient of normal restitution, e_n, which is the ratio between the pre- and post-collisional relative velocity of the colliding particles. There is no relative tangential velocity since the particles are assumed to be 'smooth'. The solid walls are modelled as frictional surfaces, and a particle colliding with a wall is analogous to a particle colliding with a particle of infinite mass, moving

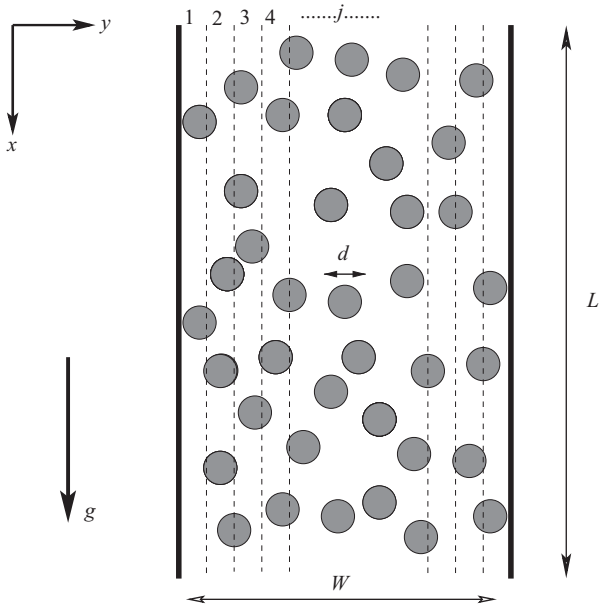

FIGURE 1. Sketch of granular Poiseuille flow. The particles are driven by gravity along the x-direction. Dotted vertical lines refer to the edges of bins that are used for binwise-averaging of particle-level properties – the first four bins are marked from the left wall.

at the velocity of the wall. The frictional properties of the walls are modelled using a single parameter, the 'tangential restitution coefficient' (β_w) for particle–wall collisions, which is defined as the fraction of relative tangential momentum transmitted from a particle to the wall during a particle–wall collision. A value of $\beta_w = 0$ corresponds to a 'rough' wall for which there is no relative tangential velocity between the particle surface and the wall upon a particle–wall collision, while $\beta_w = 1$ corresponds to a fully 'smooth' wall; another extreme value of $\beta_w = -1$ refers to a 'perfectly rough wall' for which the tangential particle velocity 'reverses' upon a particle–wall collision. It is straightforward to verify that a colliding particle retraces its path in the backward direction after its collision with a wall if $\beta_w = -1$ and $e_w = 1$ – this is referred to as the 'bounce-back' scheme which is routinely used to reproduce 'no-slip' boundary conditions in atomistic simulations of Newtonian fluids as we shall see later. The normal restitution coefficient for particle–wall collisions is assumed to be unity ($e_w = 1$) in this work.

2.2. *Event-driven simulation and averaging method*

The above particle- and wall-collision models have been implemented in the event-driven algorithm of Lubachevsky (1991) in the present simulation of granular Poiseuille flow (GPF). Because the mean-field quantities in GPF vary across the channel width, all quantities were calculated via 'binwise-averaging' by dividing the channel width into a number of bins (see figure 1), parallel to the flow direction, with the width of each bin being approximately one particle diameter. The following averaging procedure has been adopted to compute mean-field quantities in each bin

(located at $y = y_j$, with $j = 1, 2, \ldots,$ being the bin number):

$$\boldsymbol{u}_i(t) = \boldsymbol{c}_i(t) - U_x(y, t)\boldsymbol{e}_x, \tag{2.1a}$$

$$U_x(y, t) = \frac{1}{N_y}\sum_{i=1}^{N_y} c_{xi}(t), \tag{2.1b}$$

$$U_x(y) = \langle U_x(y, t)\rangle, \tag{2.1c}$$

$$\nu(y) = \left\langle \frac{\pi}{4}d^2\frac{N_y}{A_y}\right\rangle, \tag{2.1d}$$

$$T_x(y) = \left\langle \frac{1}{N_y}\sum_{i=1}^{N_y} u_{xi}(t)^2\right\rangle, \tag{2.1e}$$

$$T_y(y) = \left\langle \frac{1}{N_y}\sum_{i=1}^{N_y} u_{yi}(t)^2\right\rangle, \tag{2.1f}$$

$$T(y) = \frac{1}{2}(T_x(y) + T_y(y)), \tag{2.1g}$$

where $\boldsymbol{c}_i(t) = (c_{xi}, c_{yi})$ is the instantaneous velocity of particle i and $\boldsymbol{u}_i(t) = (u_{xi}, u_{yi})$ is its fluctuating/peculiar velocity, $U_x(y = y_j, t)$ is the instantaneous mean velocity in the jth bin located at $y = y_j$ (see figure 1), $N_y = N_y(t)$ is the number of particles in the jth bin, A_y is the area of the jth bin, $\boldsymbol{e}_x$ unit vector along the x-direction, and $\langle ...\rangle$ represents a time average. Analogous to molecular gases, the random velocity associated with particles is used to define the granular temperature T in (2.1*e*)–(2.1*g*). Note that the x- and y-components of granular temperature have been separately defined in (2.1*e*)–(2.1*f*) since T is known to be anisotropic in granular gases (Sela & Goldhirsch 1998; Alam & Luding 2003, 2005); see the Appendix for some results on temperature anisotropy and its bimodal shape.

To characterize the present GPF, five non-dimensional parameters are needed: the mean particle volume fraction (ν), the coefficient of normal restitution (e_n), the wall roughness (β_w), the channel width (W/d) and the channel length or the aspect ratio (L/W). The mean volume fraction

$$\nu = \frac{\pi N}{4\,(L/W)\,(W/d)^2}, \tag{2.2}$$

is varied by changing either the total number of particles (N) or the physical dimensions of the system. The wall roughness is controlled by choosing a specific value of the wall–particle tangential restitution coefficient, $-1 \leqslant \beta_w < 1$.

2.3. *Steady GPF and code validation*

To know whether the system has reached a steady state, we monitored the temporal evolution of the total kinetic energy of all particles:

$$E(t) = \frac{1}{2N}\sum_{i=1}^{N} c_{xi}^2 + c_{yi}^2, \tag{2.3}$$

and typical time traces of $E(t)$ are displayed in figure 2 for four values of mean density. It is seen that $E(t)$ fluctuates around some statistical mean value for each case. For a driven system like our GPF, this statistical steady state corresponds to a 'non-equilibrium' steady state (NESS) for which the streamwise velocity (U_x), volume

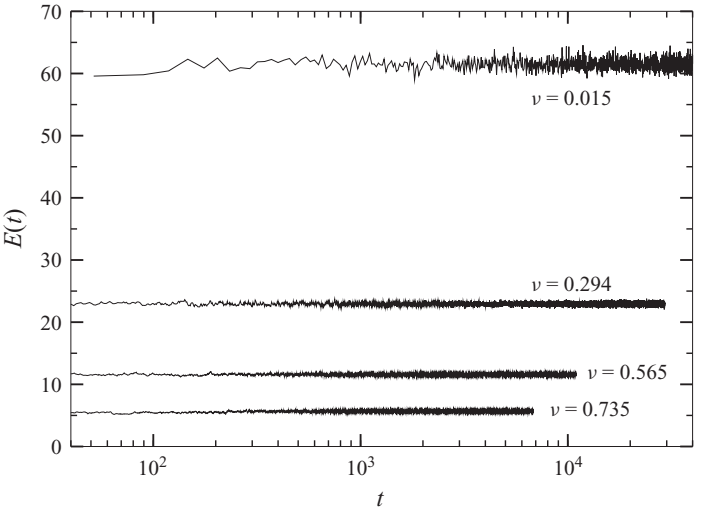

FIGURE 2. Evolution of kinetic energy of all particles with time for four different mean densities with $e_n = 0.99$, $\beta_w = 0.9$, $W/d = 31$ and $N = 900$.

fraction (ν) and granular temperature (T) also remain invariant in time (see § 3.1), having spatial variations along the wall-normal direction (y).

The constancy of $E(t)$ or the time invariance of all mean-field quantities in steady ($\partial/\partial t(\cdot) = 0$) and fully developed ($\partial/\partial x(\cdot) = 0$) granular Poiseuille flow results from the balance between the work done by the gravity and the energy loss due to particle–particle and wall–particle collisions. This NESS is reached after a long enough time (figure 2) for any dissipation ($e_n < 1$) and wall roughness ($\beta_w < 1$). In contrast to the gravity-driven Poiseuille flow of elastic particles ($e_n = 1$) for which a thermostat is required to achieve a steady state, the inherent collisional dissipation of granular particles plays the role of a thermostat in the present simulations.

One way to validate our simulation code is to compute the stresses and the related transport coefficients and compare them with theory. This has been done in our recent paper (Chikkadi & Alam 2009) where we have calculated the pressure and shear stress in GPF and compared the simulation data with a Navier–Stokes-level constitutive model. The agreement between simulation and theory was found to be almost exact in the quasi-static limit ($e_n \to 1$). In particular, the pressure (p) and shear stress (Π_{xy}) were found to be almost constant and linearly varying, respectively, across the channel width (except near the walls) in conformity with Navier–Stokes-level theory (since $\partial p/\partial y = 0$ and $\partial \Pi_{xy}/\partial y = -\varrho g$, where $\varrho = \rho_p \nu$ is the mass density of granular material, ρ_p is the intrinsic (material) density of granular material and g is the gravitational acceleration). For details on the results on the rheology of GPF, we refer the readers to Chikkadi & Alam (2009). In the present paper, we mainly focus on probing the particle-level properties of GPF, namely, the velocity distribution function and the density and velocity correlations.

All the measurements were carried out by collecting data once the flow has reached a statistically steady state as discussed above. All quantities have been made dimensionless using the reference length, velocity and temperature scales as W, $(gW)^{1/2}$ and gW, respectively. For most simulations, we have used $N = 900$ particles and a channel width of $W/d = 31$ and the length of the channel (L/W) has been

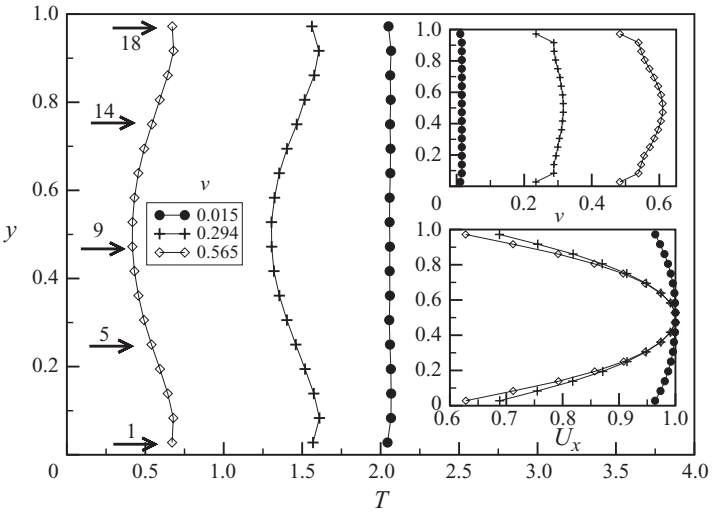

FIGURE 3. Mean velocity (U_x), granular temperature (T) and density (ν) profiles across the width of the channel at $e_n = 0.99$ and $\beta_w = 0.9$ for different mean densities. The arrows near the left ordinate indicate the locations of some bins.

varied to change the mean density (ν, see (2.2)). Here onwards, we will use volume fraction and density to designate the same quantity ν.

3. Velocity distributions in quasi-elastic limit: effects of wall roughness and density

In this section, we probe the effects of wall roughness (β_w) on velocity distribution functions for a range of mean densities, $0.015 \leqslant \nu \leqslant 0.565$, with particle collisions being quasi-elastic ($e_n = 0.99$). We will present results for three specific values of $\beta_w = 0.9$, 0.1 and -1 that correspond to 'smooth', 'rough' and 'perfectly rough' walls, respectively.

3.1. *Smooth walls*

First, we present results for 'smooth walls' by setting $\beta_w = 0.9$, with 'quasi-elastic' ($e_n = 0.99$) particle collisions. For these parameters, the mean-field quantities such as granular temperature (T), mean velocity (U_x) and particle volume fraction (ν) are shown in figure 3. They develop considerable gradients along the y-direction with increasing density and this is more pronounced for U_x, especially for dense flows, see the lower inset in figure 3. (Note that the velocity has been rescaled further by its centreline velocity such that $U_x(y) \equiv U_x(y)/U_x(y = 0.5)$.) The shear layer (i.e. the region in which the shear rate, $\mathrm{d}U_x/\mathrm{d}y$, is finite) extends upto the channel centreline even at $\nu = 0.565$. The granular temperature decreases monotonically with increasing mean density at any location; the temperature profile becomes distinctly 'bimodal' at moderate densities, with its maxima being located a little away from each wall. Further discussion on the issue of bimodal temperature profile is deferred to § 3.3.

Because the mean-field quantities of GPF have considerable gradients across the wall-normal direction, a localized, binwise study of velocity distribution functions is presented in the following. Such a localized study of velocity distributions is needed since the deviation of a velocity distribution from its leading-order Gaussian distribution is always quantified in terms of gradients of all hydrodynamic fields in

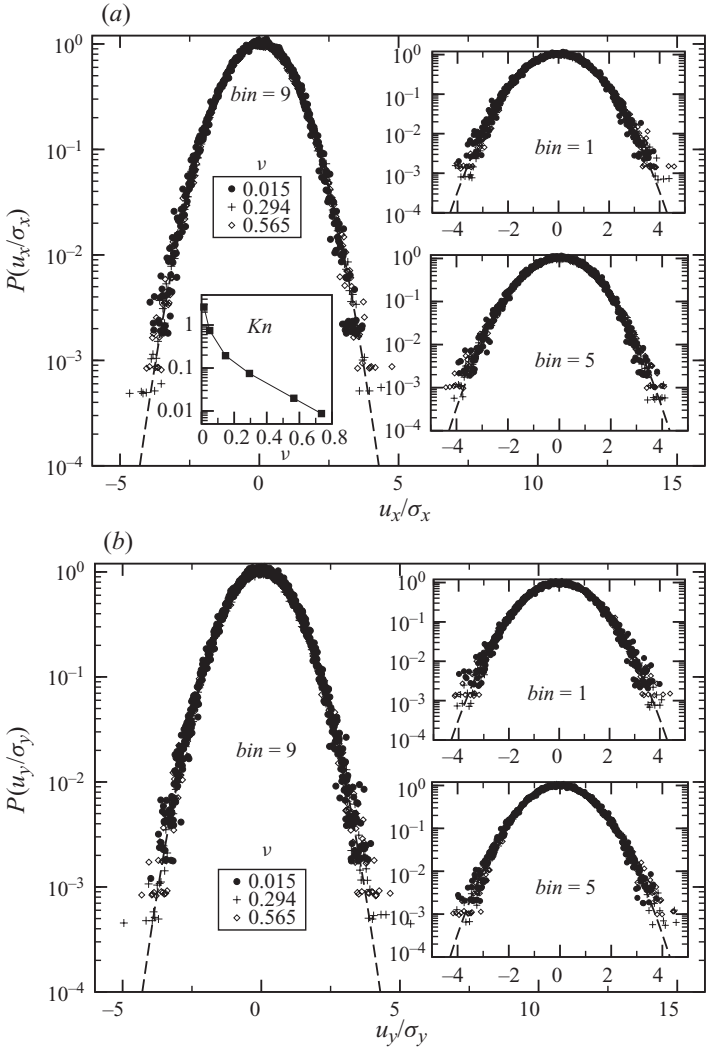

FIGURE 4. Distribution functions of (*a*) u_x and (*b*) u_y for a range of volume fractions in the quasi-elastic limit ($e_n = 0.99$) for smooth ($\beta_w = 0.9$) walls in different bins. Main panel: $bin = 9$, upper inset: $bin = 1$ and lower inset: $bin = 5$. The dashed curve in each panel indicates a Gaussian. Left inset in (*a*) shows the variation of Knudsen number, *Kn*, with volume fraction.

Chapman–Enskog-type expansion of the pertinent kinetic equation. In the present study, the number of bins used for a channel width of $W/d = 31$ is 18; most of the simulations were repeated by using an increased number of bins (30) which did not affect the presented results as we shall demonstrate later. For the ease of understanding, the location of few bins are indicated by arrows in figure 3, with $bin = 1, 18$ being located adjacent to the walls, $bin = 5, 14$ in the shear layer and $bin = 9, 10$ around the centre of the channel.

Figures 4(*a*) and 4(*b*) show the probability distribution functions of the fluctuating streamwise velocity (u_x) and transverse fluctuating velocity (u_y), respectively, for dilute-to-dense flows ($0.015 \leqslant \nu \leqslant 0.565$) in different bins. The local (binwise) distribution functions on only one side of the channel centreline are presented

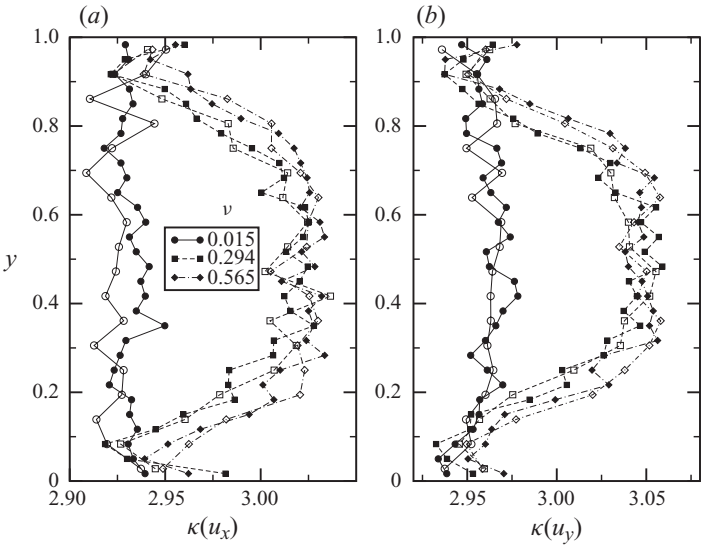

FIGURE 5. Kurtosis (κ) of (a) $P(u_x)$ and (b) $P(u_y)$ distributions for the parameter values given in figure 4. The open and filled symbols correspond to calculations with 18 and 30 bins, respectively.

as the distributions on the other side are the same; however, in some cases, the distributions on both sides are presented when they differ. In each plot, the horizontal axis has been scaled by the variance of the distribution function $\sigma_i = \sqrt{\langle u_i^2 \rangle}$, where the index i denotes the coordinate direction, and the vertical axis has been scaled such that $P(0) = 1$. It is observed that both the u_x and u_y distribution functions in all bins remain close to a Gaussian for a wide range of densities. In order to quantify how close these distributions are to a Gaussian, the kurtosis of the distribution is computed:

$$\kappa(u_i) = \frac{\mu_4(u_i)}{\mu_2(u_i)^2}, \tag{3.1}$$

where

$$\mu_\alpha(u_i) = \int_{-\infty}^{\infty} (u_i - \langle u_i \rangle)^\alpha P(u_i)\, \mathrm{d}u_i \tag{3.2}$$

is the αth moment about the mean of the distribution. The variation of the kurtosis of $P(u_x)$ and $P(u_y)$ distributions with y is shown in figures 5(a) and 5(b), respectively, for the parameter values of figure 4. The open and filled symbols in figure 5 refer to calculations with 18 and 30 bins, respectively, and the results remain insensitive to the number of bins used. It is clear that there are systematic deviations of the kurtosis of each distribution from its Gaussian value of 3. For the dilute case ($\nu = 0.015$), the kurtosis is almost uniform in all bins, with $\kappa(u_x) \approx 2.93$ and $\kappa(u_y) \approx 2.96$. For denser flows ($\nu = 0.294$ and 0.565), $\kappa(u_x)$ and $\kappa(u_y)$ are close to 3.02 and 3.05 in the bulk, respectively, and gradually decrease to 2.95 near the wall.

From the results in this section for a range of volume fractions covering dilute to dense flows, the kurtosis is found to be $\kappa(u_i) \approx 3(\pm 2\,\%)$, and hence the velocity distribution functions in GPF are indeed close to Gaussian in the quasi-elastic limit for smooth walls.

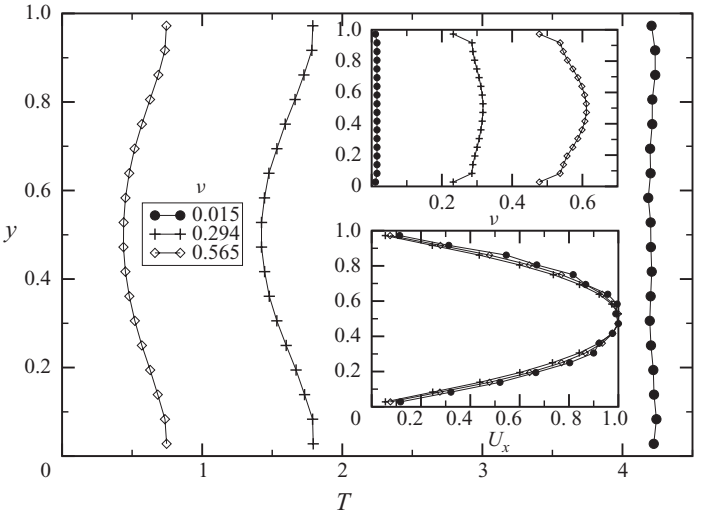

FIGURE 6. Same as figure 3, but for perfectly rough walls ($\beta_w = -1$).

3.2. *Perfectly rough walls ($\beta_w = -1$)*

Recall that a 'perfectly' rough wall is characterized by a wall–particle tangential restitution coefficient of $\beta_w = -1$ for which the tangential component of particle velocity 'reverses' upon a particle–wall collision. The previous work (Vijayakumar & Alam 2007) did not probe any wall roughness of $\beta_w < 0$, and hence the following results for $\beta_w = -1$, which closely resemble those for smooth walls ($\beta_w = 1$), are briefly discussed. It is worth pointing out that the collisional dissipation due to wall roughness is proportional to $(1 - \beta_w^2)$ and hence vanishes in the limiting cases of perfectly smooth ($\beta_w \to 1$) and rough ($\beta_w \to -1$) walls.

The profiles of mean fields for $\beta_w = -1$, as displayed in figure 6, look similar to those for smooth walls in figure 3. The velocity profile in the lower inset of figure 6 indicates that a 'no-slip' condition holds at a perfectly rough wall ($\beta_w = -1$), which is in contrast to the large values of wall slip for smooth walls (see figure 3). The former result suggests that the well-known 'bounce-back' scheme (where the particle retraces its path after its collision with the wall) could reproduce the no-slip boundary condition for a granular fluid too.

For $\beta_w = -1$, the probability distributions of fluctuating velocities, $P(u_x)$ and $P(u_y)$, are shown in figures 7(a) and 7(b), with the corresponding variations of kurtosis in figures 8(a) and 8(b), respectively. From these two sets of figures, we find that, as in the case of smooth walls ($\beta_w = 0.9$), both $P(u_x)$ and $P(u_y)$ distributions are indeed close to a Gaussian from dilute to dense regimes of GPF with perfectly rough walls ($\beta_w = -1$).

The gradients of mean fields ($\mathrm{d}U_x/\mathrm{d}y$, $\mathrm{d}\nu/\mathrm{d}y$ and $\mathrm{d}T/\mathrm{d}y$) for perfectly rough and smooth walls are compared in figure 9 for three representative values of mean density ($\nu = 0.015$, 0.294 and 0.565). The wall roughness does not seem to have noticeable effect on both density and temperature gradients as it is clear from figure 9(*b, c, e, f, h, i*). In contrast, the shear rate ($\mathrm{d}U_x/\mathrm{d}y$) can differ by at least a factor of two when the walls are made perfectly rough ($\beta_w = -1$).

The effect of mean-field gradients on distribution functions can now be assessed. Note that the kurtosis values of distribution functions for $\beta_w = 0.9$ and -1 differ at

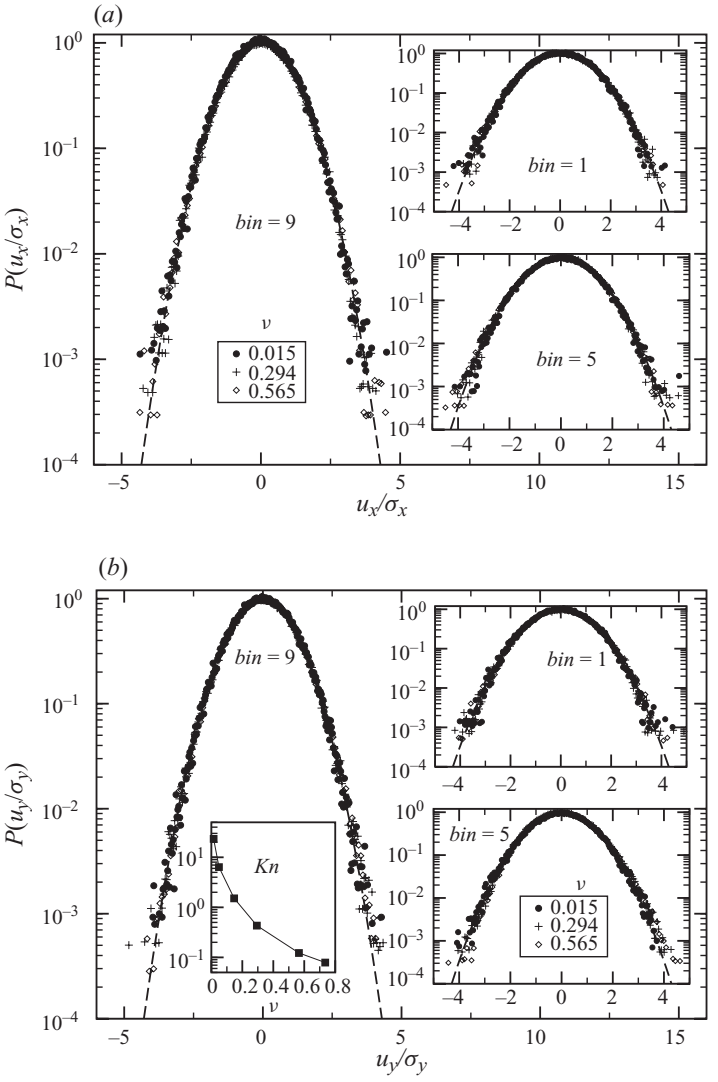

FIGURE 7. Same as figure 4, but for perfectly rough ($\beta_w = -1.0$) walls. Main panel: $bin = 9$, upper inset: $bin = 1$ and lower inset: $bin = 5$. The dashed curve in each panel indicates a Gaussian. Left inset in (b) shows the variation of Knudsen number with mean density.

most by 1 % which is evident from a comparison between the dashed line ($\beta_w = -1$) and the dashed line with squares ($\beta_w = 0.9$) in figure 8 at a mean density of $\nu = 0.294$ – similar trends hold at other mean densities. The interesting observation is that even though the mean velocity field has large gradients for both smooth and perfectly rough walls, they do not have noticeable effects on kurtosis and hence on the form of 'local' velocity distribution functions.

For both smooth and perfectly rough walls, the variations of the Knudsen number, $Kn = \lambda/W$, the ratio between the mean free path and the channel width, with mean density are shown in the left inset of figures 4(a) and 7(b). It is seen that Knudsen number increases with decreasing ν and becomes of $O(1)$ for $\beta_w = 0.9$ and $O(10)$ for $\beta_w = -1$ in the dilute limit. Following the well-known flow classification in terms of

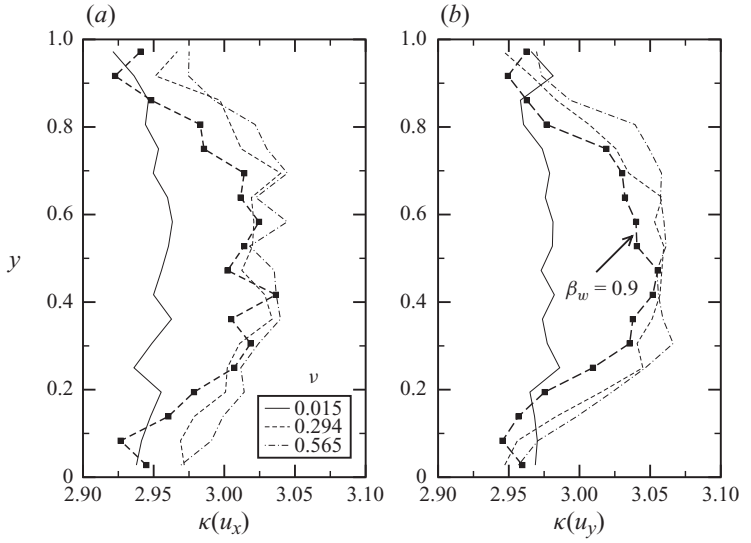

FIGURE 8. Kurtosis ($\kappa(u_i)$) of (*a*) $P(u_x)$ and (*b*) $P(u_y)$ distributions for perfectly rough walls ($\beta_w = -1.0$) with $e_n = 0.99$. The dashed line with filled squares corresponds to $\kappa(u_i)$ for $\nu = 0.294$ with smooth walls ($\beta_w = 0.9$).

Knudsen number (Karniadakis & Besok 2001), we can conclude that our GPF is in the 'transitional flow' ($0.1 < Kn < 10$) regime for $\nu < 0.3$ and in the 'slip-flow' regime ($0.01 < Kn < 0.1$) for $\nu > 0.3$. That the distribution functions are indeed close to a Gaussian is a surprising result, especially in the dilute limit that corresponds to the transitional flow regime. Looking at the deviations of kurtosis values from a Gaussian in figures 5 and 8, it is clear that the corrections to the leading-order Gaussian due to 'large' Knudsen numbers are small, suggesting that the higher-order effects in dilute rarefied GPF could be small.

All the above conclusions hold for GPF as long as the walls are 'smooth' ($\beta_w \sim 1$) or 'perfectly rough' ($\beta_w \sim -1$) and the particle collisions are 'quasi-elastic' ($e_n \sim 1$).

3.3. *Rough walls*

In our previous work (Vijayakumar & Alam 2007), we have found that a wall roughness of $\beta_w \sim 0$ introduces interesting asymmetric features in the probability distribution for the streamwise velocity. This is depicted in figure 10 for the probability distribution of the instantaneous streamwise velocity c_x in $bin = 1$ for $\nu = 0.015$, note the sharp peak in the low velocity region. Since the particles lose significant amount of tangential velocity on colliding with a 'rough' wall in comparison with their collisions with a 'smooth' wall, a peak near the low velocity region is expected for rough walls. The greater the loss of tangential velocity at walls, the stronger the deviation is from a Gaussian. The inset in figure 10 clearly shows that $P(c_x)$ approaches a Gaussian with increased wall smoothness (i.e. with increasing value of β_w), and hence the observed asymmetry of $P(c_x)$ is a wall-roughness-induced phenomenon.

For rough walls with $\beta_w = 0.1$, the mean-field quantities in the quasi-elastic limit ($e_n = 0.99$) are shown in figure 11. In comparison to the results for smooth walls in figure 3, the gradients of all mean-field quantities for rough walls are much larger, which is due to the greater amount of dissipation of energy for wall–particle collisions. As in the case of smooth walls, the shear layer extends upto the channel centreline, and the granular temperature profile is 'bimodal' for dense flows. Note that the

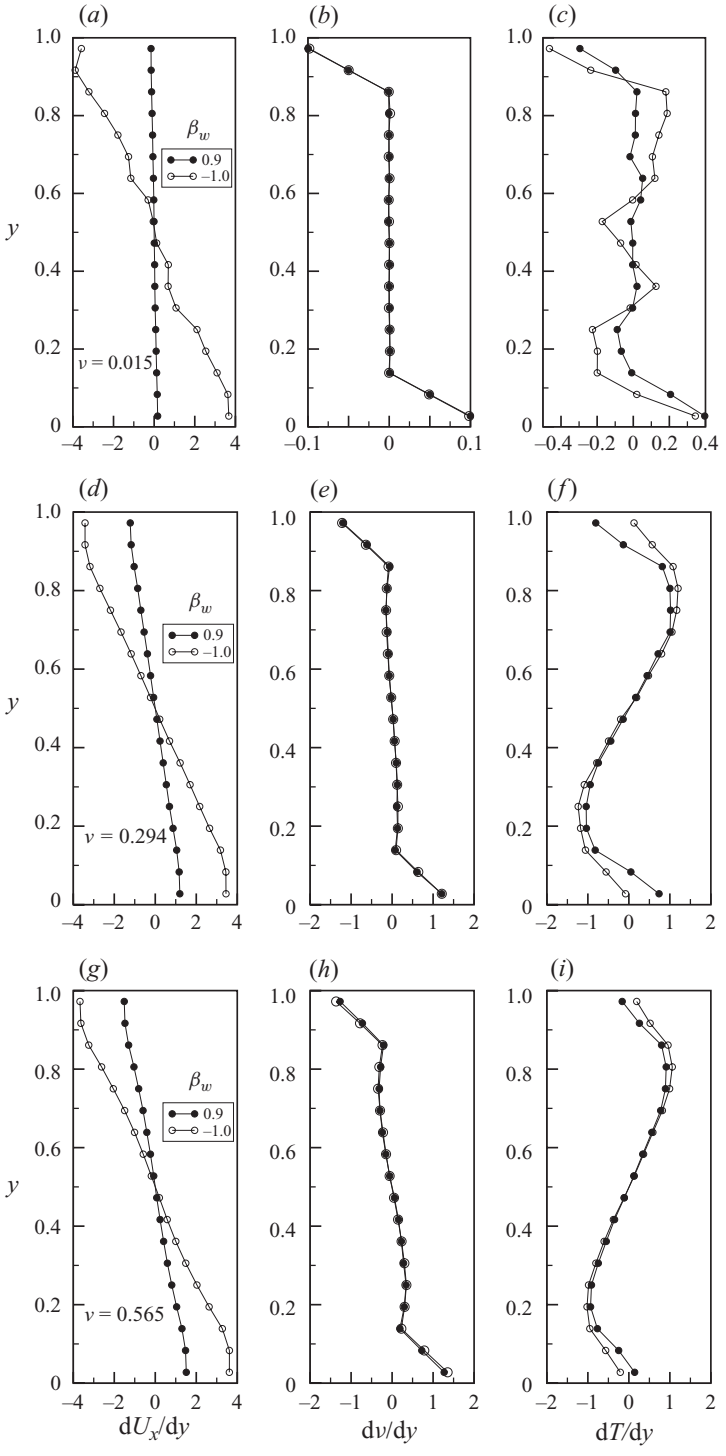

FIGURE 9. Effects of wall roughness on the gradients of mean fields at $e_n = 0.99$: (*a–c*) $\nu = 0.015$; (*d–f*) $\nu = 0.294$; (*g–i*) $\nu = 0.565$. (*a, d, g*) Shear rate (dU_x/dy); (*b, e, h*) density gradient ($d\nu/dy$); (*c, f, i*) temperature gradient (dT/dy). Filled and open symbols represent smooth ($\beta_w = 0.9$) and perfectly rough ($\beta_w = -1.0$) walls, respectively.

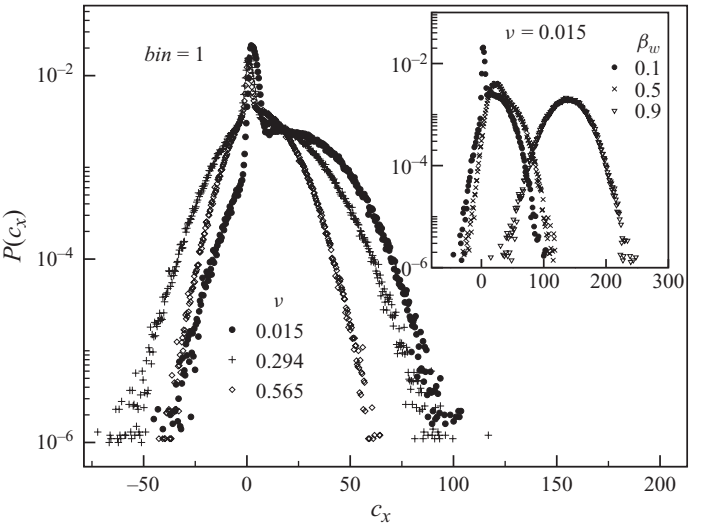

FIGURE 10. Main panel, distribution function for the streamwise component of the 'instantaneous' particle velocity, c_x, for a range of volume fractions in the quasi-elastic limit ($e_n = 0.99$) for rough ($\beta_w = 0.1$) walls in $bin = 1$. Inset, distribution of c_x in $bin = 1$ for a range of wall roughness.

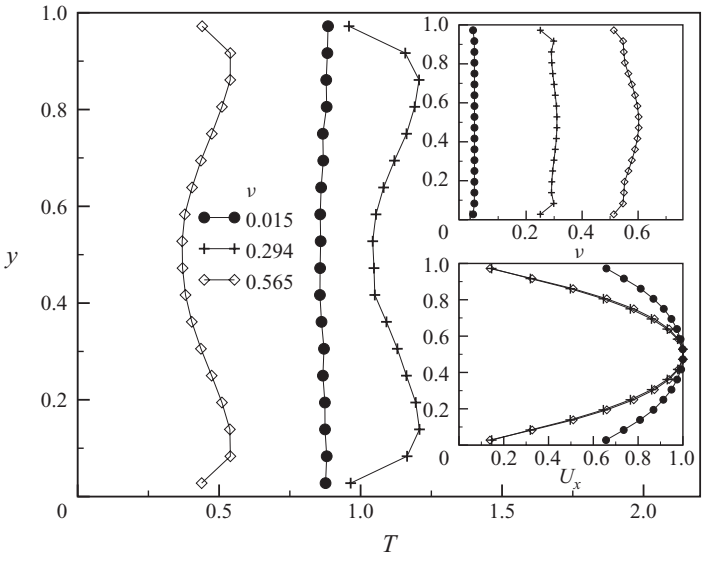

FIGURE 11. Same as figure 3, but for rough walls ($\beta_w = 0.1$).

thickness of the temperature boundary layer near the walls and the temperature maxima are larger for the rough wall case in comparison to those for smooth walls (figure 3). Another noteworthy difference with the smooth wall case is that the granular temperature varies non-monotonically with density: T increases with increasing density, reaches a maximum at some intermediate density and thereafter decreases in the same limit. Since the Knudsen number is large for dilute flows ($Kn \sim O(5)$ at $\nu = 0.015$ with $\beta_w = 0.1$), the wall–particle collisions dominate over particle–particle collisions, and hence the temperature would largely be determined

by a balance between the dissipation of energy due to wall–particle collisions and the production of energy due to shearing. It has been verified that the dissipation due to wall–particle collisions ($\sim (1-\beta_w^2)$) increases by an order of magnitude when β_w is decreased from 0.9 to 0.1. Since the average granular temperature is inversely proportional to the total (wall + bulk) collisional dissipation, the temperature for dilute flows with $\beta_w = 0.1$ is expected to be much lower than that for smooth walls $\beta_w = 0.9$. With increasing density, Kn decreases and hence the energy dissipation due to particle–particle collisions becomes increasingly larger and would eventually dominate over that for wall–particle collisions beyond some critical density, leading to the observed non-monotonicity of the granular temperature with density (main panel of figure 11).

It is worth pointing out that the kinetic theory analysis of dilute granular Poiseuille flow by Tij & Santos (2004) uncovered a similar bimodal shape of the temperature profile that appears at the level of second-order correction in terms of Knudsen number and the bimodality disappears at the Navier–Stokes order of their theory. Clearly, their prediction of bimodal granular temperature in dilute GPF is a Burnett-order effect and does not depend on wall roughness. In contrast to the results of Tij & Santos (2004), we found that the bimodality of granular temperature in our simulations of narrow channels becomes prominent for moderately dense to dense flows; the height of this temperature maxima is largest when the walls are rough ($\beta_w \sim 0$) and the temperature maxima shift towards the wall as the walls are made perfectly smooth ($\beta_w \to 1$) or perfectly rough ($\beta_w = -1$). Recall that the collisional dissipation due to wall–particle collisions is maximum for $\beta_w = 0$ and zero for $\beta_w = \pm 1$. The added loss of energy due to wall–particle collisions (for $\beta_w \neq \pm 1$) is responsible for a 'lower' temperature at the walls (and a 'higher' temperature away from the walls), resulting in the 'bimodality' of granular temperature, and the temperature maxima shifts towards the wall when $\beta_w \to \pm 1$. Therefore, the bimodality of the granular temperature in our simulations is primarily controlled by the wall-roughness-induced dissipation and hence a wall effect.

With parameter values as in figure 11, the probability distribution functions of streamwise and transverse fluctuation velocities ($P(u_x)$ and $P(u_y)$) are shown in figures 12(a) and 12(b), respectively, for a range of densities in three bins. Near the wall ($bin = 1$, main panel), the asymmetric single-peak structure in $P(u_x)$, with its peak being positioned at some negative velocity, persists at all densities. However, near the centreline ($bin = 9$, upper inset) and a little away from the left wall ($bin = 5$, lower inset), $P(u_x)$ remains asymmetric only at low densities and becomes a Gaussian at larger densities. The near-wall ($bin = 1$) distribution function of $P(u_y)$ (main panel of figure 12b) displays a 'bimodal double-peak' structure in the dilute limit ($\nu = 0.015$), but is Gaussian at higher densities ($\nu = 0.294, 0.565$); however, $P(u_y)$ in the bulk ($bin = 9, 5$ in upper and lower insets) remains Gaussian at any density.

The effect of wall roughness on $P(u_x)$ and $P(u_y)$ distributions in $bin = 1$ is shown in figures 13(a) and 13(b), respectively. For the sake of clarity, we have only displayed the low-velocity region of each distribution function in figure 13. It is clear that, as in the case of the distribution for the instantaneous particle velocity $P(c_x)$ in figure 10, the asymmetry in $P(u_x)$ diminishes with increasing wall smoothness as seen in the main panel of figure 13(a). Similarly, the height of the double-peak structure in $P(u_y)$ diminishes in the same limit as seen in the main panel of figure 13(b). The insets in each panel further indicate that the asymmetry of $P(u_x)$ and the bimodal structure of $P(u_y)$ vanish in the limit of perfectly rough walls too. In either case, the respective distribution function eventually approaches a Gaussian distribution when the walls

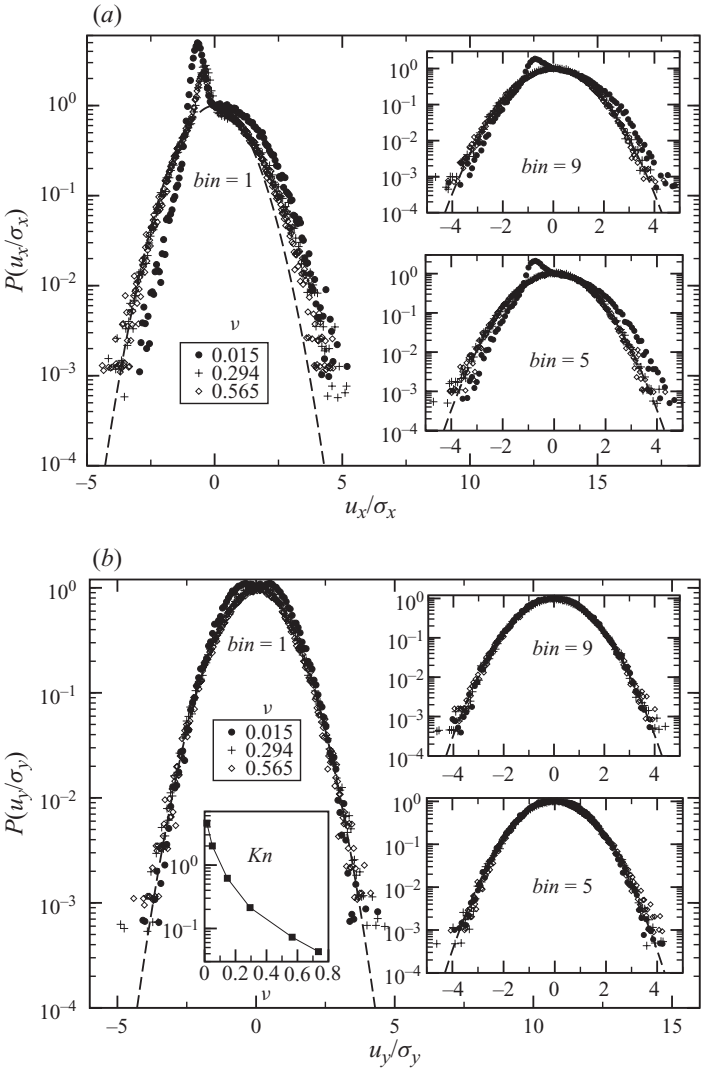

FIGURE 12. Velocity distribution functions for rough walls ($\beta_w = 0.1$) with $e_n = 0.99$. Main panel: $bin = 1$, upper inset: $bin = 9$, lower inset: $bin = 5$. Left inset in (b) displays the variation of Knudsen number with mean density. The dashed line in each panel indicates a Gaussian.

are made perfectly smooth ($\beta_w \to 1$) or perfectly rough ($\beta_w \to -1$); note that the dissipation due to wall–particle collisions vanishes in both limiting cases ($\beta_w \to \pm 1$). Therefore, the observed asymmetry of $P(u_x)$ and the bimodal shape of $P(u_y)$ are due to the wall-induced-dissipation and hence wall effects.

The variations of the kurtosis of $P(u_x)$ and $P(u_y)$ are shown in figures 14(a) and 14(b), respectively, with parameter values as in figure 12. Again, the results remain relatively insensitive when the number of bins is increased from 18 (open symbols) to 30 (filled symbols). The deviation of $P(u_x)$ distribution from a Gaussian is apparent from the binwise kurtosis of distributions in figure 14(a). It is clear that $\kappa(u_x)$ deviates from its Gaussian value of 3 in all the bins for dilute flows ($\nu = 0.015$), but only in the wall region for moderate ($\nu = 0.294$) and dense ($\nu = 0.565$) flows.

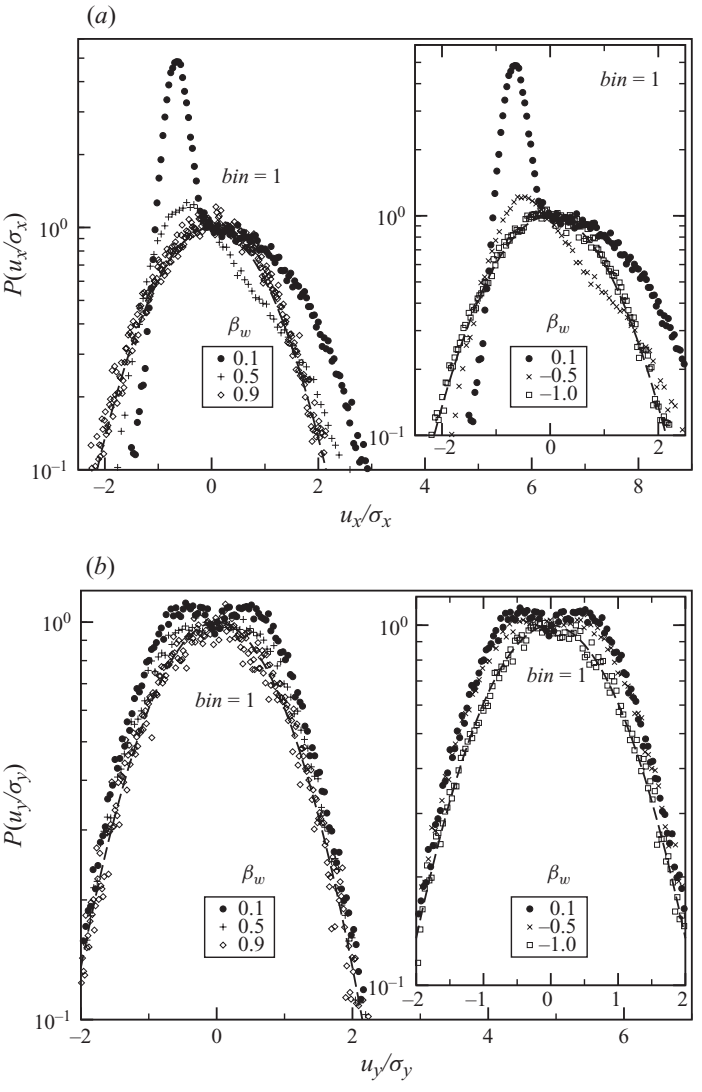

FIGURE 13. Effect of wall roughness (β_w) on the distributions of (*a*) $P(u_x)$ and (*b*) $P(u_y)$ in $bin = 1$ for dilute flows ($\nu = 0.015$). Main panel: $\beta_w = 0.9$, 0.5 and 0.1; inset: $\beta_w = -1$, -0.5 and 0.1.

Similarly, the kurtosis of $P(u_y)$ distribution in figure 14(*b*) remains close to 3 ± 0.05 at higher densities ($\nu = 0.294$, 0.565), but significantly lower than 3 for dilute flows ($\nu = 0.015$), especially near the wall where a bimodal double-peak structure was seen (figure 12*b*).

Remarkably, even though the gradients of hydrodynamics fields are much larger for rough walls in comparison to smooth walls, the deviation of the $P(u_y)$ distribution from a Gaussian (in terms of its Kurtosis $\kappa(u_y)$) is relatively smaller (compare figure 14*b* with figure 5*b*). This suggests that the hydrodynamic gradients have a minor role on the form of the distribution functions for 'quasi-elastic' collisions, and it is the 'wall roughness' that plays a crucial role on the distribution functions of GPF in the quasi-elastic limit.

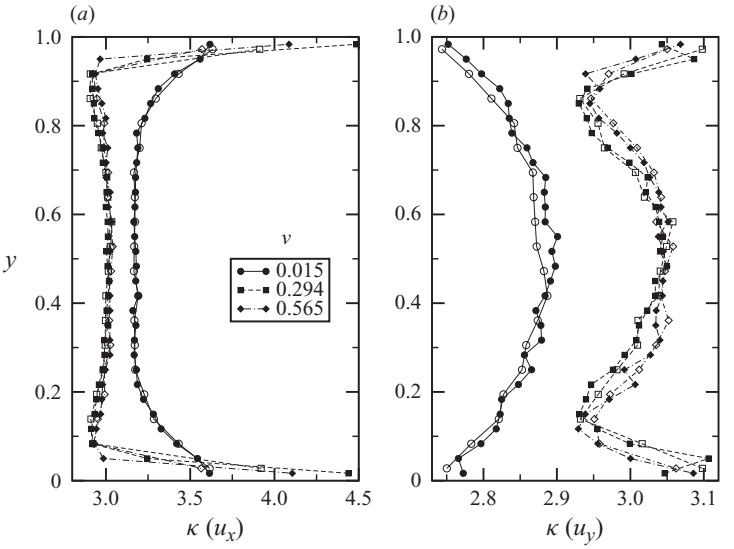

FIGURE 14. Kurtosis ($\kappa(u_i)$) of (*a*) $P(u_x)$ and (*b*) $P(u_y)$ distributions for the parameter values given in figure 12. The open and filled symbols correspond to calculations with 18 and 30 bins, respectively.

Lastly, to check the dependence of the presented results on the system size, some of the simulations were repeated by increasing the number of particles (N) and the channel width (W/d). From a comparison of the results (not shown) for dilute flows ($\nu = 0.015$) with rough walls ($\beta_w = 0.1$) with $N = 900$ and $N = 3600$ ($W/d = 31$ and $W/d = 62$, respectively), we found that both $P(u_x)$ and $P(u_y)$ remain invariant, and the wall-roughness-induced asymmetry in the $P(u_x)$ distribution persists even for larger systems and is not an artifact of simulation.

4. Velocity distributions at higher dissipation

In this section, the effects of dissipation and wall roughness on the velocity distribution are probed for dense flows. We begin our study by probing the distribution functions at moderate densities in § 4.1 and then move to very high densities in § 4.2. Because the characteristics of distribution functions are found to be similar for both smooth ($\beta_w \sim 1$) and perfectly rough walls ($\beta_w \sim -1$), henceforth we will present results for two specific values of $\beta_w = 0.9$ and 0.1 that correspond to 'smooth' and 'rough' walls, respectively.

4.1. *Moderately dense flows and the effect of density waves*

It is well known that an increase in the degree of dissipation gives rise to the formation of clusters which can significantly affect various properties of the system. Especially, at moderate densities where density waves become prevalent with increasing dissipation and system size (Liss, Conway & Glasser 2002; Alam, Chikkadi & Gupta 2010), we will try to quantify the effect of clustering on velocity distributions in GPF.

The particle volume fraction is fixed at $\nu \sim 0.3$ to study moderately dense flows. A series of snapshots of particle positions in the steady state for three values of the coefficient of restitution e_n are shown in figure 15 for smooth walls ($\beta_w = 0.9$). Particles are almost uniformly distributed across the channel at $e_n = 0.99$, but at $e_n = 0.9$ and 0.8 the flow becomes 'inhomogeneous' along both x- and y-directions.

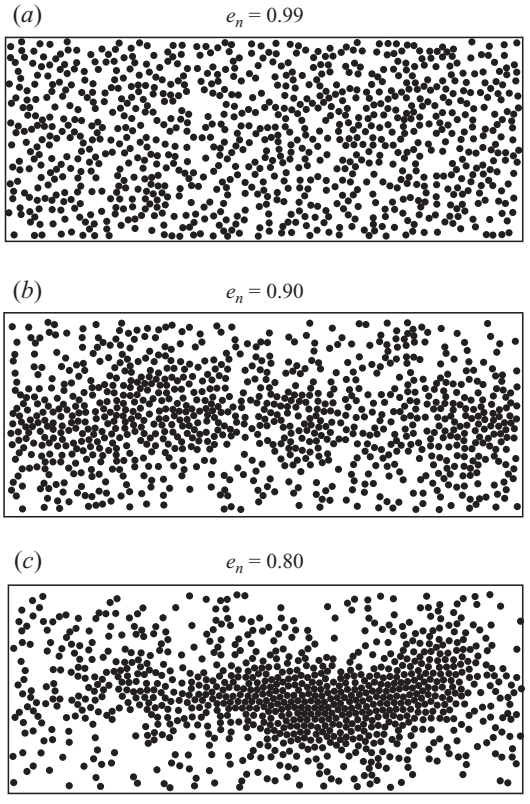

FIGURE 15. Snapshots of particle positions in the steady state at $\nu = 0.294$ and $\beta_w = 0.9$ for different e_n. The flow is from left to right along the direction of gravity.

The appropriate way to analyse such an inhomogeneous system is to use a 'cell-wise' averaging method wherein the channel is divided into a number of cells (of size $\delta x \times \delta y$) and then the distribution functions are calculated in each cell. However, one must be careful while performing averaging since the averaging needs to be carried out only over those cells in which the mean fields and their gradients have the same values – this is a tedious and time-consuming exercise and is left to a future study. Instead, we follow the earlier described binwise averaging method: even though our binwise (along y-direction) study of distribution functions cannot take into account the effects of density inhomogeneities along the x- direction (e.g. at $e_n = 0.8$), here our main aim is to pinpoint the possible effects of such streamwise inhomogeneities on the local, binwise distribution functions.

In figures 16(a) and 16(b), the $P(u_x)$ and $P(u_y)$ distributions for the parameter values of figure 15 are shown. As we increase dissipation, the $P(u_x)$ distribution becomes asymmetric in all bins (except near the wall, see the upper inset of figure 16a for $bin = 1$, where it is close to a Gaussian even at $e_n = 0.8$) having a deviated 'negative' tail, with a larger probability of negative velocities. Clearly, the negative fluctuation velocities u_x decay at a slower rate in comparison with their positive counterparts with increasing dissipation. The $P(u_y)$ distribution in figure 16(b) becomes asymmetric too with increasing dissipation; however, in contrast to $P(u_x)$, its asymmetry changes sign about the channel centreline. For example, consider the $P(u_y)$ distribution in $bin = 5$

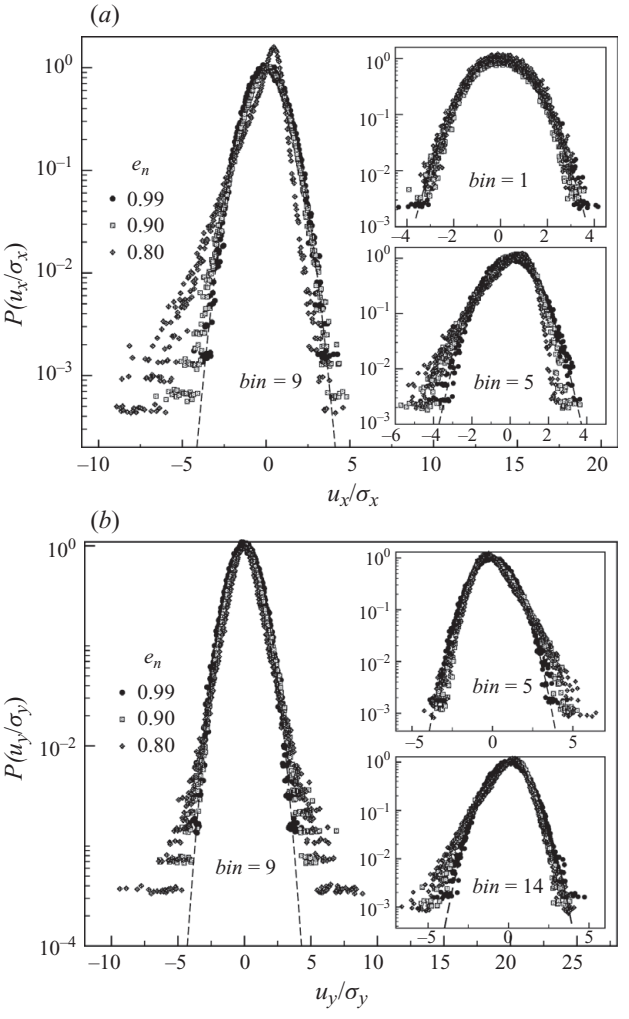

FIGURE 16. Effect of restitution coefficient, e_n, on (*a*) $P(u_x)$ and (*b*) $P(u_y)$ at a mean density $\nu = 0.294$ for smooth walls ($\beta_w = 0.9$).

and $bin = 14$ that are shown in the upper and lower insets of figure 16(*b*), respectively. These bins are located symmetrically about the centre of the channel (refer to bin locations in figure 3), and the distributions have asymmetries in opposite directions. This is expected since the particle velocity c_y gets reversed upon a wall–particle collision.

A study of density waves in a gravity-driven channel flow was carried out recently (Liss *et al.* 2002; Alam *et al.* 2010). The corresponding phase diagram shows three different kinds of density waves: plug, wave and slug/clump, over a range of volume fractions ($\nu = 0.05$–0.5) in the steady state. Figure 17 displays such steady-state density waves at a volume fraction of $\nu = 0.294$, with $e_n = 0.85$ and $W/d = 31$; the channel length L/W and the particle number N were varied to obtain different structures. The structure at $L/W \sim 1$ resembles a plug, a sinuous wave at $L/W \sim 2$ and a slug at $L/W > 3$. It is important to know the way these structures affect the mean fields and the velocity distributions. Surprisingly, the profiles of mean-field quantities

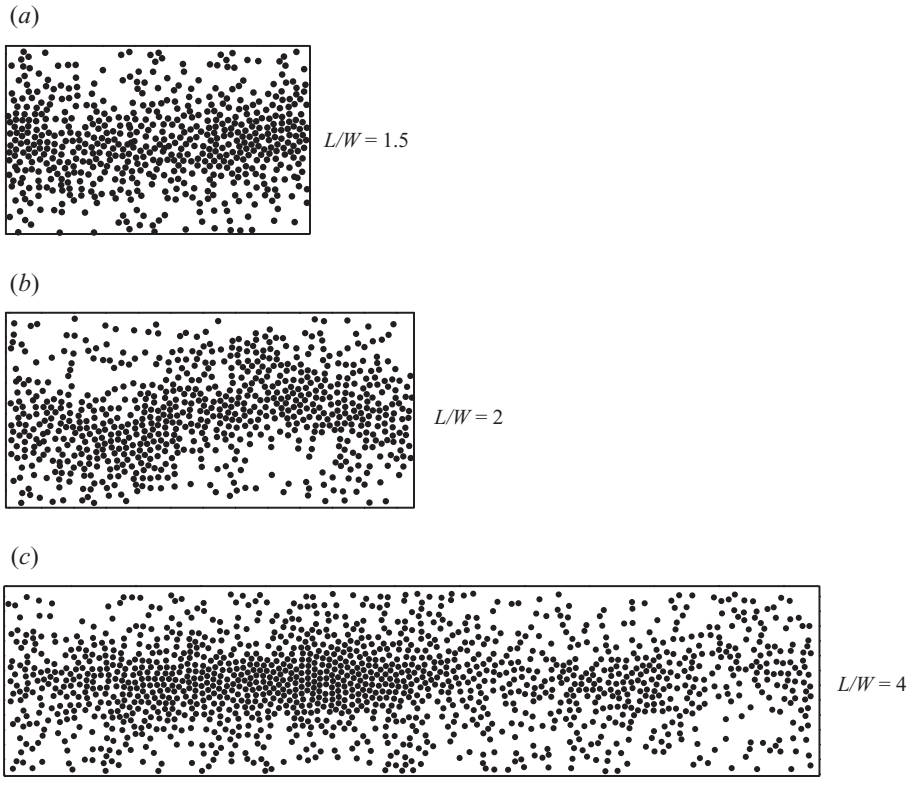

FIGURE 17. Effect of channel length (L/W) on the steady-state structures at $\nu \sim 0.30$, $e_n = 0.85$ and $\beta_w = 0.9$.

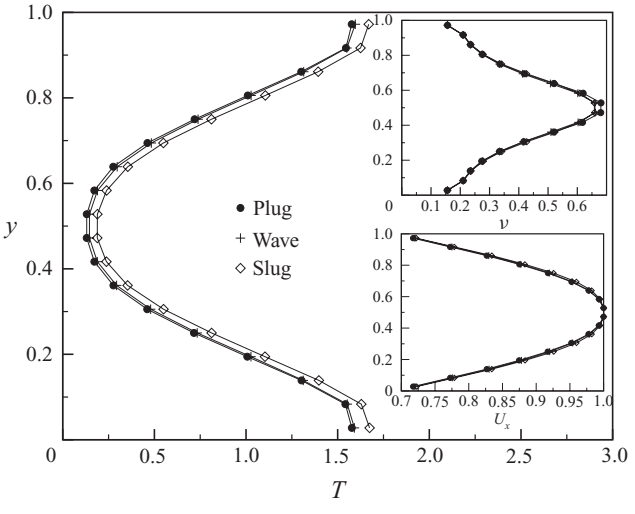

FIGURE 18. Mean velocity (U_x), granular temperature (T) and volume fraction (ν) profiles across the width of the channel for different steady states with parameter values as in figure 17.

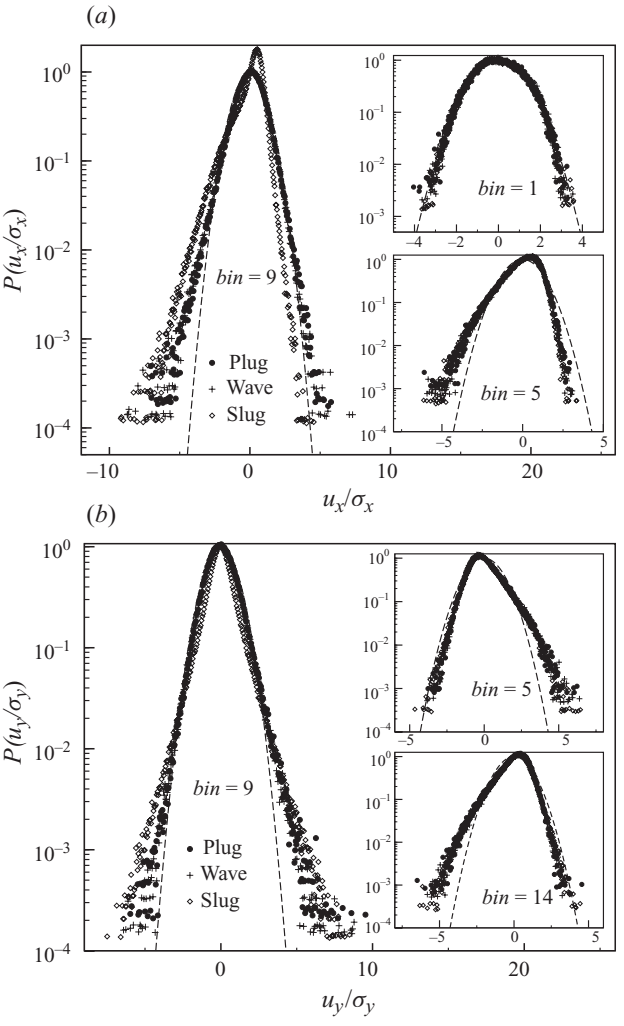

FIGURE 19. Effect of density waves on (*a*) $P(u_x)$ and (*b*) $P(u_y)$ for parameter values as in figure 17.

in figure 18 are almost identical for the three types of density waves, except for the granular temperature in the case of a slug ($L/W = 4$) that shows a marginally increased value at any location across the channel.

The corresponding velocity distribution functions $P(u_x)$ and $P(u_y)$ are shown in figure 19. The overall characteristics of both $P(u_x)$ and $P(u_y)$ resemble those in figure 16 for $L/W = 2$ with $e_n = 0.8$. Interestingly, the asymmetry associated with $P(u_x)$ distributions at the channel centreline (main panel in figure 19*a*) and in the shear layer (lower inset in figure 19*a*) for a slug is much stronger in comparison to that for a plug or a sinuous wave. For the $P(u_y)$ distributions in figure 19(*b*), we see that the distributions in the shear layers remain relatively unaffected by a plug/wave/slug, but the distributions around the channel centreline are strongly affected (main panel in figure 19*b*) and become more non-Gaussian in the presence of a slug.

We conclude that the increased dissipation leads to asymmetric velocity distribution functions for both $P(u_x)$ and $P(u_y)$. The emergence of density waves (sinuous

wave/slug) with increased channel length makes these asymmetries stronger, especially in the presence of a slug. In either case, however, the near-wall distribution functions remain relatively unaffected and are close to a Gaussian for smooth walls. We shall return to discuss the above asymmetry issue in § 4.3 for very dense flows and characterize them in terms of the skewness of distributions.

4.2. *Highly dense flows and non-Gaussian tails*

The particle volume fraction is varied from $\nu = 0.5$ to 0.85 to study the velocity distributions at high densities. In our previous work (Vijayakumar & Alam 2007), we had probed velocity distribution functions in GPF upto a maximum density of $\nu = 0.56$. In the present paper, we consider very large densities upto $\nu = 0.85$ that are relevant in most experimental works in GPF; we will quantify the high-velocity tails of distributions and the effect of various control parameters (restitution coefficient, wall roughness, etc.) on them for a range of densities in the dense limit.

First, we focus on very high densities, above the square-packing density of $\nu = \pi/4$. So far a square lattice has been used for initializing the particle positions and the maximum mean density that could be obtained was $\nu \sim 0.78$. To simulate very high density flows i.e. $\nu > \pi/4$, the particles are assigned positions on a triangular lattice. A maximum density of $\nu \sim 0.9$ could be achieved this way. The mean-field quantities at $\nu = 0.85$ for smooth ($\beta_w = 0.9$) and rough walls ($\beta_w = 0.1$) are shown in figures 20(a) and 20(b), respectively; for this case, the number of particles is $N = 1225$, with $W/d = 31.2$ and $L/d = 36.2$. We see that the shear layer outside the dense plug region is very thin, confined to only a few bin widths from the walls, and the wall roughness makes it even thinner, i.e. for $\beta_w = 0.1$. For quasi-elastic collisions ($e_n = 0.99$) the density within the plug region remains lower than the maximum packing limit, irrespective of the wall roughness; with increasing inelastic dissipation, however, the density reaches close to its maximum limit there. Therefore, the inelastic dissipation helps to increase the spatial ordering of particles in the plug. This observation holds for other values of mean density ν, and a more quantitative measure of this dissipation-induced ordering is given in § 5 via pair correlation functions. Note that all hydrodynamic fields are nearly uniform and their gradients are close to zero within the plug.

At $\nu = 0.85$, the effect of restitution coefficient on the velocity distributions, $P(u_x)$ and $P(u_y)$, in different bins for smooth walls ($\beta_w = 0.9$) is shown in figure 21. The velocity distribution in $bin = 1$ (adjacent to the wall), the upper inset in figure 21(a), remains close to a Gaussian, irrespective of the value of e_n. The $P(u_x)$ distribution in $bin = 2$ (in the shear layer), the lower inset in figure 21(a), becomes non-Gaussian with overpopulated tails and 'asymmetric' with increasing dissipation. This asymmetry in $P(u_x)$ with increasing dissipation persists near the channel centreline ($bin = 9$ in the main panel in figure 21a). The asymmetry of $P(u_x)$, with a relatively larger probability for negative velocities, indicates that the decay rate of the large negative streamwise velocity fluctuations u_x is lower than their positive components (along the direction of gravity). Therefore, the gravity helps to enhance the decay rate of positive streamwise velocity fluctuations, thereby leading to the observed asymmetry of the $P(u_x)$ distribution.

The transition of $P(u_y)$ at the channel centreline ($bin = 9$, figure 21b) with increasing dissipation is very similar to that seen in $P(u_x)$, with the major difference that the tails of $P(u_y)$ remain almost symmetric. The distribution in $bin = 1$ remains Gaussian and is not shown here; instead we include the distribution in $bin = 17$, which is symmetrically located about the channel centreline with respect to $bin = 2$. The $P(u_y)$ distributions in these two bins are mirror images, and, as discussed before for the moderately

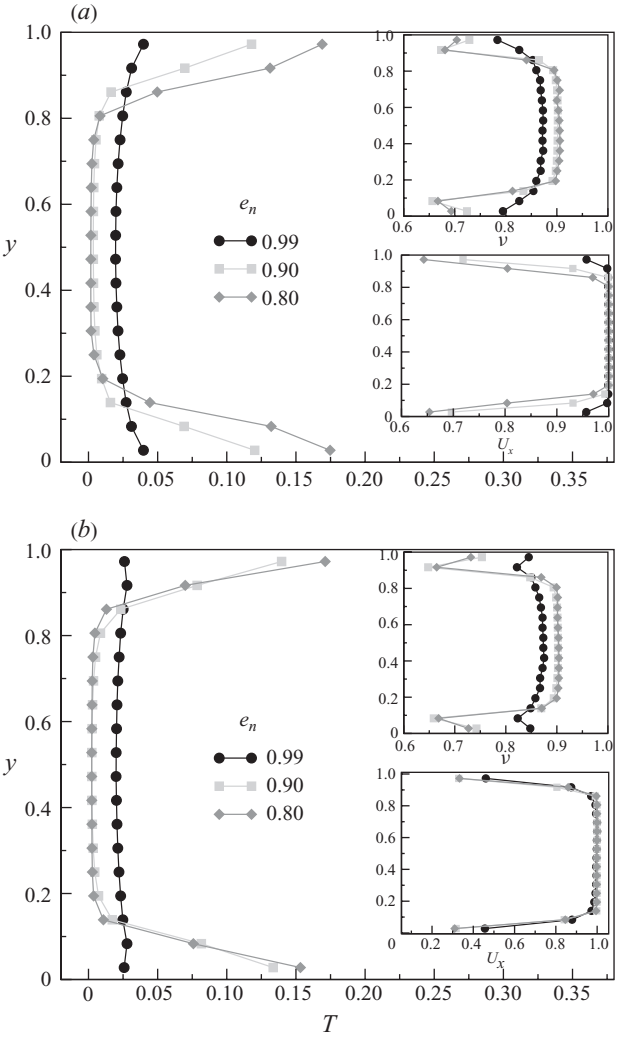

FIGURE 20. Mean-field quantities U_x, T and ν for an ultra-dense flow $\nu = 0.85$ with (a) smooth ($\beta_w = 0.9$) and (b) rough ($\beta_w = 0.1$) walls. Other parameters are $N = 1225$, $W/d = 31.2$ and $L/d = 36.2$.

dense case, the asymmetry of $P(u_y)$ is expected due to the underlying symmetry of the transverse velocity about the channel centreline. In either case, the distributions become non-Gaussian with overpopulated tails with increasing dissipation.

An analogue of figure 21(a) is shown in figure 22 for the $P(u_x)$ distribution for rough walls ($\beta_w = 0.1$). The behaviour of distribution functions in $bin = 9$ (main panel) and $bin = 2$ (lower inset) looks similar to that for smooth walls ($\beta_w = 0.9$) in figure 21(a). However, as in the dilute flows, the $P(u_x)$ distribution in $bin = 1$ (upper inset) carries the distinct signature of wall roughness that shows up as a dominant peak for small negative velocities. It is noteworthy that this negative peak vanishes in $bin = 2$ (lower inset), suggesting that the effect of wall roughness remains confined to a very small region near the wall at $\nu = 0.85$.

An analogue of figure 21 for a relatively lower density flow ($\nu = 0.565$) is displayed in figure 23 that shows the effects of e_n on the forms of $P(u_x)$ and $P(u_y)$ distributions

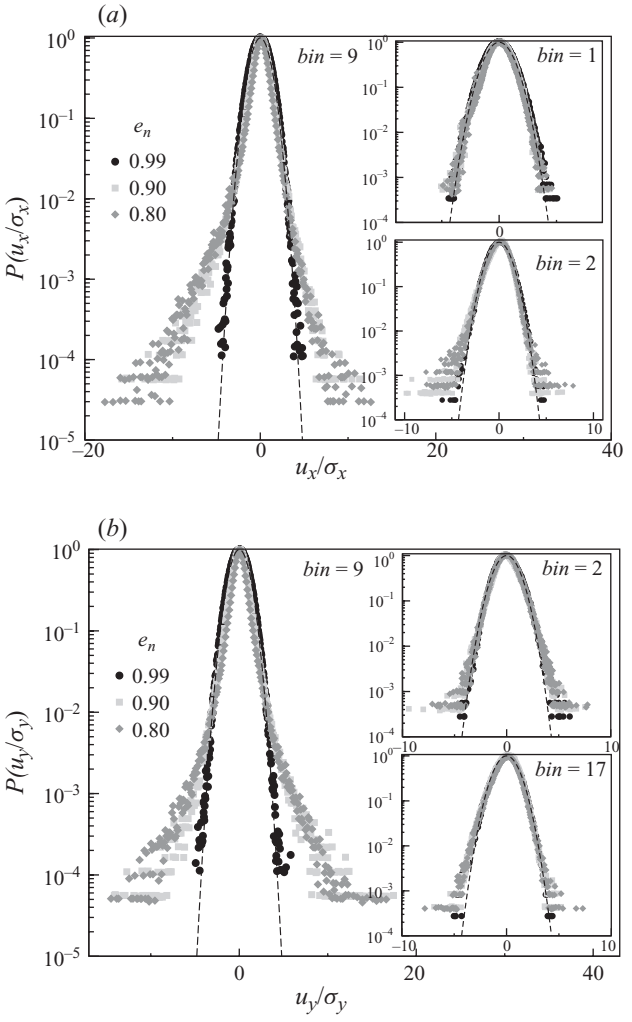

FIGURE 21. Effect of restitution coefficient, e_n, on (*a*) $P(u_x)$ and (*b*) $P(u_y)$ at $\nu = 0.85$ for smooth walls ($\beta_w = 0.9$).

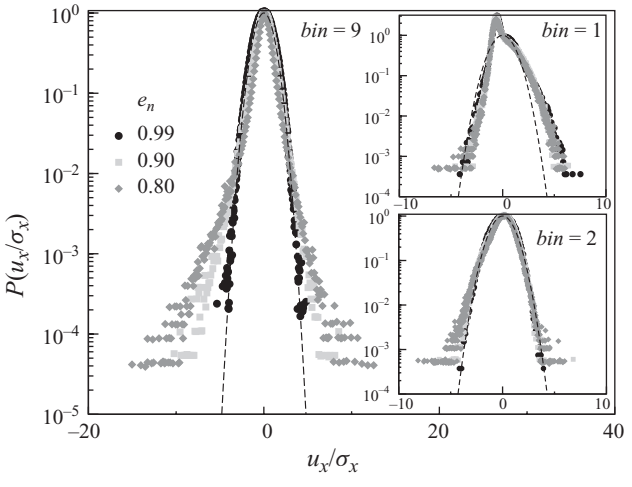

FIGURE 22. Same as figure 21(*a*), but rough walls ($\beta_w = 0.1$).

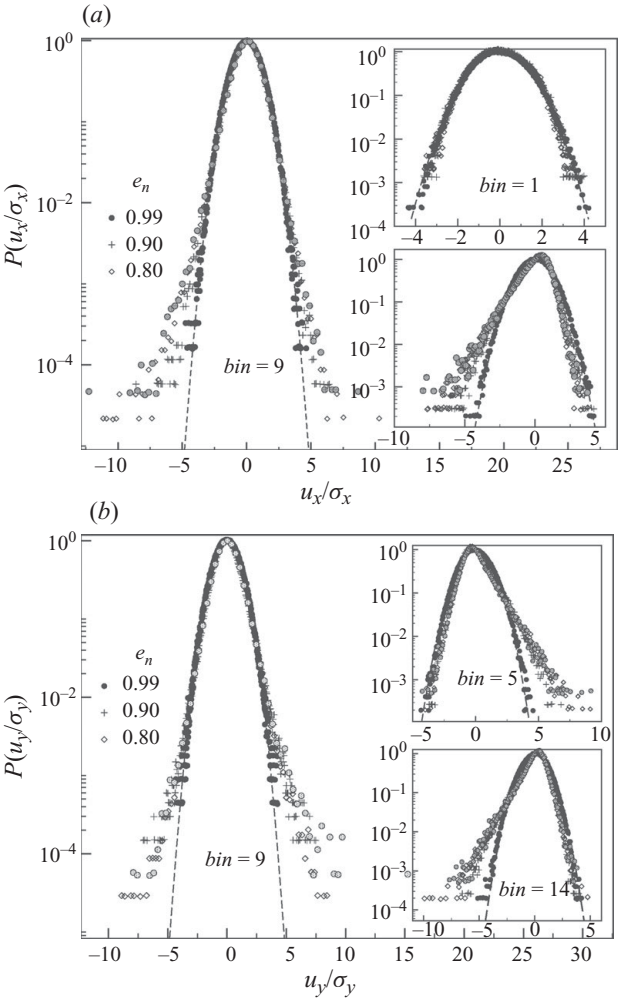

FIGURE 23. Effect of restitution coefficient, e_n, on (*a*) $P(u_x)$ and (*b*) $P(u_y)$ at $\nu = 0.565$, $N = 7200$, $W/d = 31$ and $L/W = 10.4$ for smooth walls ($\beta_w = 0.9$). The grey circles in each panel represent data for a smaller system with $N = 900$ and $W/d = 31$ for $e_n = 0.8$.

in different bins. (Since the shear layer is relatively thicker at $\nu = 0.565$, we have shown the velocity distributions in $bin = 5$ and $bin = 15$ instead of $bin = 2$ and $bin = 17$ for $\nu = 0.85$.) Overall, the transition of $P(u_x)$ and $P(u_y)$ with e_n in different bins is qualitatively similar to the one for the densest flow studied $\nu = 0.85$, but the deviation of tails from Gaussian is relatively larger (i.e. more overpopulated) for denser flows. Note that most of the data presented in figure 23 correspond to a large system of $N = 7200$ (circles, pluses and diamonds); the grey circles correspond to a smaller system size of $N = 900$ and $W/d = 31$ at $e_n = 0.8$. It is clear that there is a good agreement between the distributions at $N = 900$ and 7200, and hence the presented results are independent of the system size. Snapshots of particle positions in steady state for $N = 900$ and $N = 7200$ particles, with other parameters as in figure 23, are shown in figure 24. At an aspect ratio of $L/W = 1.3$ ($N = 900$), we see a plug formation around the channel centreline in figure 24(*a*); the inhomogeneities in the plug along the x-direction are negligible even when the aspect ratio $L/W = 10.4$ ($N = 7200$) is

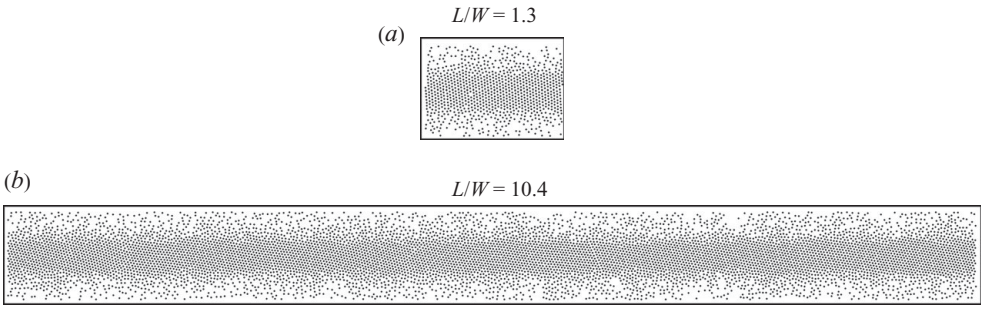

FIGURE 24. Snapshots of particle positions in the steady state for $\nu = 0.565$, $e_n = 0.8$, $\beta_w = 0.9$ and $W/d = 31$ when (*a*) $N = 900$ and (*b*) $N = 7200$ particles.

increased eightfold as observed in figure 24(*b*). The invariance of both $P(u_x)$ and $P(u_y)$ distributions for different system sizes at $e_n = 0.8$ is due to the invariance of the underlying flow structure (i.e. a plug) for $L/W = 1.3$ and 10.4 (and hence with system size N).

4.2.1. *High-velocity tails and comparison with experiments*

For a range of particle volume fractions studied in the dense regime with $\nu > 0.5$, we find that the tails of $P(u_i)$ in the plug region can be fitted via a power law of the form $P(u_i) \sim u_i^{-\alpha_i}$. This is evident from figures 25(*a*) and 25(*b*) for $\nu = 0.565$ with smooth walls ($\beta_w = 0.9$); the results for rough walls and higher densities are similar. The inset in the upper panel displays the variation of the power-law exponent α_x with e_n, with α_+ and α_- denoting exponents for positive and negative velocity tails, respectively. At larger dissipation, the exponent α_x appears to saturate to a constant value for $e_n < 0.85$; this near-constancy of α_i could be due to the fact that the density within the plug saturates to the close-packing limit ($\nu_c \sim 0.9$) for $e_n < 0.85$ (the other hydrodynamic fields and their gradients also remain invariant there with a further decrease in e_n). Therefore, this weak variation of α_i with e_n for $e_n < 0.85$ could be tied to the slow variation of all hydrodynamic fields and their gradients. A comparison between the exponents for the high-velocity tails at $\nu = 0.85$ (not shown) and $\nu = 0.565$ indicates a slower decay of large velocities with increasing mean density.

Before making a comparison with experimental data, we must note here that we do not have clean data for very high velocities and the tails span only over a limited range of three decades. Therefore, our observations on power-law tails are not conclusive; rather our data are a starting point for future theoretical study which could shed further light on the possibility of power-law tails in GPF.

Interestingly, a power-law behaviour for the tails of $P(u_x)$ and $P(u_y)$ distribution functions has recently been reported in experiments on Poiseuille-type granular flow (Moka & Nott 2005), and the corresponding power-law exponents varied over a range of $\alpha \sim 2.9$–7.4. This is similar to our simulation results within the dense plug. However, there is a difference between our results and those obtained from these experiments: the experiments showed that the distribution functions in the plug region (where the hydrodynamic gradients are negligible) are the same as in the shear layer (where the shear rate varies sharply); in contrast, our simulations showed that the distribution functions in the plug region are markedly different from those in the shear layer. Note that in experiments (Moka & Nott 2005) the shear rate varies sharply inside the shear layer but the density variation is negligible there; however, in simulations we found considerable density variation inside the shear layer along with

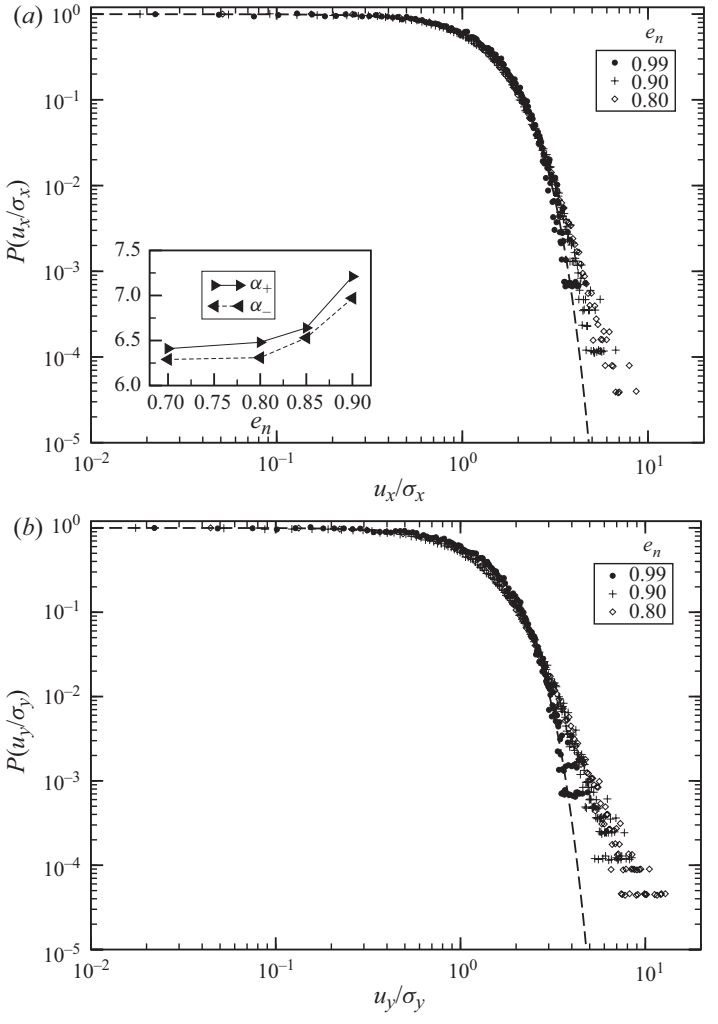

FIGURE 25. Log-log plots of (*a*) $P(u_x)$ and (*b*) $P(u_y)$ in $bin = 9$ for $\nu = 0.565$ with smooth walls ($\beta_w = 0.9$). The inset in (*a*) displays exponents of the positive (α_+) and negative (α_-) velocity tails of $P(u_x)$ distributions.

other hydrodynamic fields, and our simulations also showed that the mean density affects the form of distribution functions significantly. Therefore, the density effect within the shear layer might be responsible for the variance between experimental and simulation distribution functions in the shear layer.

Apart from our simplistic collision model of smooth inelastic hard disks, the experimental protocols also differ from our simulations in three ways:

(i) The experimental geometry is a quasi-two-dimensional channel having a spanwise width of a few particle diameters, with particles exiting through a sieve at the bottom of the channel. This is in contrast to our 'periodic' simulations along the x-direction. It is anticipated that the 'back flows' originating from the stagnation zones around the sieve at the bottom of the channel are likely to affect the particle motion in the bulk which remain unexplored.

(ii) Experimental measurements are essentially 'surface' measurements of particle velocity near the 'smooth' front glass wall. The effects of such front and back walls on the particle motion remains unknown since the particle properties in the bulk have not been probed. In contrast, the simulated system is assumed to be uniform along the spanwise direction and hence our data represent measurements in the bulk.

(iii) Experiments have been carried out with spheres, but our two-dimensional simulations are for disks. It is known that the non-Gaussianity of distribution functions could also depend on the dimensionality of the problem.

In order to make a direct comparison with experiments, all the above ingredients of the particle collision model as well as the geometry of the experimental set-up need to be incorporated in simulations. Despite these differences, the qualitative behaviour of distribution functions within the dense plug remains similar in experiments and simulations.

4.3. *Asymmetric tails and the skewness of distributions*

The tails of $P(u_x)$ and $P(u_y)$ distributions develop asymmetry with increasing collisional dissipation, which is evident from figures 21–23 for highly dense flows ($\nu = 0.565$ and 0.85). We have also found in §4.1 that such asymmetries of $P(u_x)$ and $P(u_y)$ develop even at a lower density, see figure 16 for $\nu = 0.3$; moreover, these asymmetries become stronger in the presence of density waves (a sinuous wave/slug); see figure 19. In this section, we quantify the effects of dissipation and mean density on the asymmetric forms of distribution functions.

A simple way to characterize the above asymmetry is to compute the skewness of the distribution, which is given by the expression:

$$\gamma(u_i) = \frac{\mu_3(u_i)}{\mu_2(u_i)^{3/2}}, \tag{4.1}$$

where $\mu_3(u_i)$ and $\mu_2(u_i)$ are the third and second moments of the fluctuating velocity u_i, respectively, as defined in (3.2). The binwise skewness of $P(u_x)$ and $P(u_y)$ distributions for $\nu = 0.565$ in figures 23(a) and 23(b) are displayed in figures 26(a) and 26(b), respectively, while the skewness of distributions for $\nu = 0.85$ in figures 21 and 22 are shown in figures 27(a) and 27(b), respectively. (For the sake of completeness, the related variations of kurtosis $\kappa(u_i)$ at $\nu = 0.565$ are displayed in figure 26(c, d) and those of shear rate and temperature gradient are displayed in figure 26(e, f), respectively.) In each figure, the continuous lines represent results for smooth walls ($\beta_w = 0.9$) and the open symbols represent those for rough walls ($\beta_w = 0.1$).

Let us focus on the skewness of the distributions at $\nu = 0.565$ in figure 26. In the quasi-elastic limit, the magnitude of skewness is close to zero in all the bins except for the $P(u_x)$ distribution in the near-wall region for rough walls. The magnitudes of $\gamma(u_x)$ and $\gamma(u_y)$ increase with increasing dissipation and vary non-monotonically along the y-coordinate. The skewness $\gamma(u_i)$ is maximum in the region where the shear rate, shown in figure 26(e), is high and minimum in the plug region where the shear rate is small. The skewness of the $P(u_x)$ distribution in figure 26(a) remains negative in all the bins, while the skewness of the $P(u_y)$ distribution in figure 26(b) changes sign because of the underlying symmetry of the u_y-velocity. These overall features of $\gamma(u_x)$ and $\gamma(u_y)$ hold for the densest flow $\nu = 0.85$ in figure 27. Note that the maximum skewness within the shear layer decreases with increasing mean density.

Figure 28 summarizes the effects of mean density on the skewness of the $P(u_x)$ distribution, $\gamma(u_x)$, near the channel centreline ($bin = 9$) at $e_n = 0.8$ for smooth walls ($\beta_w = 0.9$). For dense flows with $\nu > 0.6$, $\gamma(u_x)$ remains almost constant, but decreases

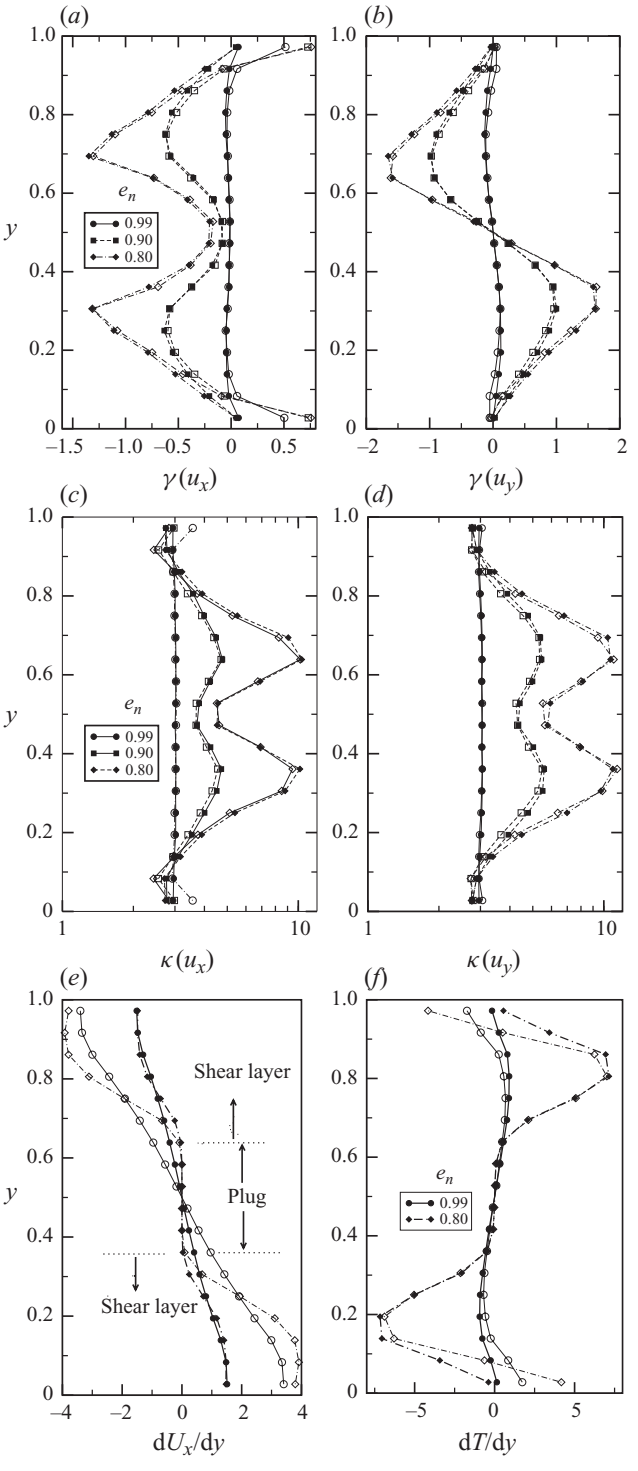

FIGURE 26. Effects of dissipation (e_n) and wall roughness (β_w) on (a,b) skewness $\gamma(u_i)$ and (c,d) kurtosis $\kappa(u_i)$ of $P(u_x)$ and $P(u_y)$ distributions at $\nu = 0.565$. (e, f) The variations of shear rate (dU_x/dy) and temperature gradient dT/dy. The open symbols represent data for rough walls ($\beta_w = 0.1$) and the filled symbols represent data for smooth walls ($\beta_w = 0.9$).

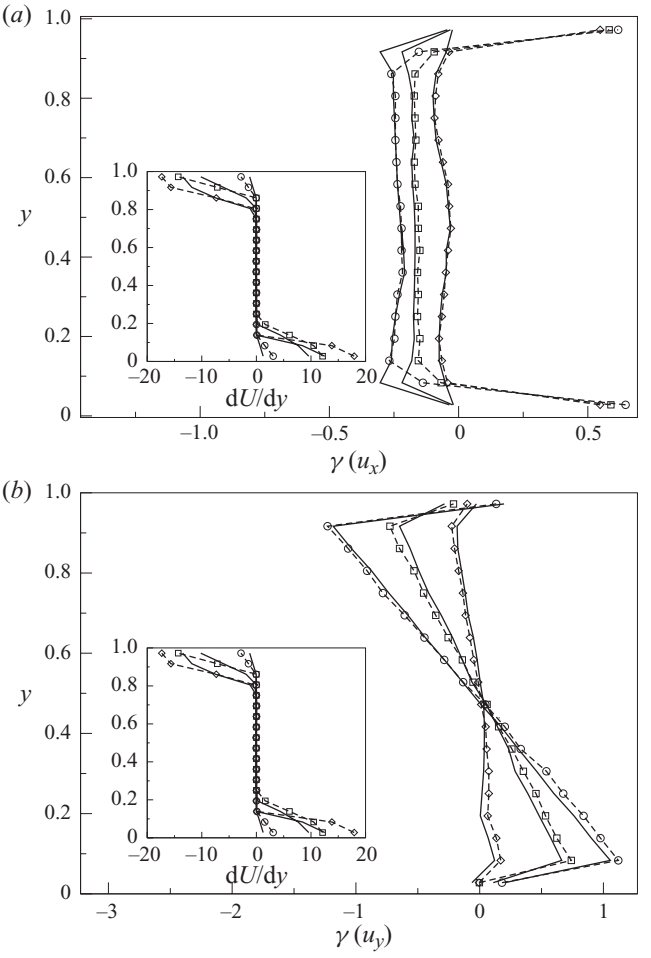

FIGURE 27. The skewness of (*a*) $P(u_x)$ and (*b*) $P(u_y)$ distributions in various bins across the channel width; insets: the shear rate variations at $\nu = 0.85$. The open symbols (diamonds, squares and circles for $e_n = 0.99, 0.9$ and 0.8, respectively) represent skewness for rough walls ($\beta_w = 0.1$) and continuous lines represent skewness for smooth walls ($\beta_w = 0.9$).

with decreasing mean density for $\nu < 0.6$. For moderately dense flows ($\nu \sim 0.3$, §4.1), the inhomogeneities/density waves along the x-direction have a dominant effect on the distributions, so the skewness is seen to attain a maximum at a density of $\nu \sim 0.3$. Below this density ($\nu < 0.3$), the prevalence of density waves (sinuous wave or plug) decreases and there is a transverse ordering of particles leading to the formation of a plug and hence the skewness decreases for $\nu < 0.3$. In the inset of figure 28, the skewness is presented as a function of the local (binwise) volume fraction $\nu_{bin} \equiv \nu(bin = 9)$. It is seen that the skewness remains constant for $\nu_{bin} > 0.85$, which corresponds to a mean density of $\nu > 0.6$. Clearly, the skewness changes little when the local density is close to its maximum packing limit since all hydrodynamic fields become nearly uniform with negligible gradients there.

5. Density and spatial velocity correlations

We have found in §4 that for dense flows the tails of velocity distributions make a transition from Gaussian to 'overpopulated' non-Gaussian with decreasing

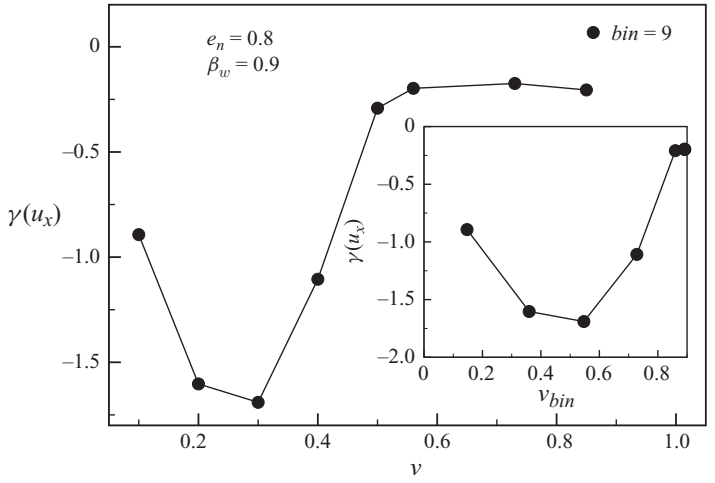

FIGURE 28. Effect of mean volume fraction on the skewness of $P(u_x)$ distribution near the channel centreline ($bin = 9$) for $e_n = 0.8$ and $\beta_w = 0.9$. In the inset, skewness is plotted as a function of the 'local' (binwise) volume fraction.

restitution coefficient (e_n). It was observed that even the low-velocity region of distributions deviates from a Gaussian at $\nu = 0.85$ and $e_n = 0.8$. It has been shown by various authors (Blair & Kudrolli 2001; Moon *et al.* 2001; Prevost, Egolf & Urbach 2002; Pouliquen 2004) that inelastic collisions lead to velocity correlations that are responsible for the non-Gaussian velocity distribution. To pinpoint the precise role of e_n on the non-Gaussianity of distribution functions in GPF, we study its effect on the pair correlation function and the spatial velocity correlations.

5.1. *Pair correlation function*

The pair correlation function $g(r)$ is defined as the probability of finding a neighbour at a distance r from a particle at the origin; thus, $g(r)$ provides a measure of local spatial ordering of the particles. In this study, $g(r)$ is always anisotropic because the deformation field of GPF is 'inhomogeneous'; therefore, we will analyse the binwise pair correlation function, $g(x, y_k)$, which is defined as

$$g(x, y_k) = \frac{2A}{N_y^2} \left\langle \sum_{i=1}^{N_y} \sum_{j>i}^{N_y} \delta(x - x_{ij}) \right\rangle, \tag{5.1}$$

where A is the area of the bin located at $y = y_k$, N_y is the number of particles in that bin and the angular bracket indicates an average over time.

We begin by examining the effect of restitution coefficient on spatial ordering at a mean density of $\nu = 0.565$ for smooth walls ($\beta_w = 0.9$). The snapshots of particle positions at $e_n = 0.99$ and $e_n = 0.8$ are displayed in figures 29(a) and 29(b), respectively. An increase in dissipation gives rise to a plug around the channel centreline, and a crystal-like ordering of particles within the plug at $e_n = 0.8$ can be discerned from figure 29(b). For a better understanding of the local structure of the fluid, we turn our attention to the pair correlation function in figure 30; in this section, we have used 30 bins (each of width of about one particle diameter) because a smaller number of bins (say, 18) leads to qualitative changes in the structure of $g(x)$, especially at higher density with large dissipation. In the quasi-elastic limit ($e_n = 0.99$), the pair correlation function (figure 30a) shows a liquid-like structure in all bins; such a liquid

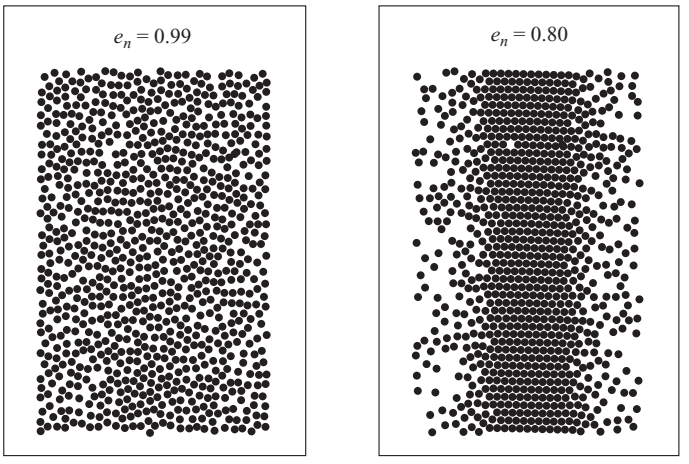

FIGURE 29. Snapshots of instantaneous particle positions at steady state for $\nu = 0.565$ and $\beta_w = 0.9$ for (*a*) $e_n = 0.99$ and (*b*) $e_n = 0.80$.

regime is expected at $e_n = 0.99$ because the particles are homogeneously distributed within the channel and the mean density is much below the square-packing density. The signature of plug formation with increasing dissipation shows up in the pair correlation function for the central $bin = 15$ in figure 30(*b*): the dominant peaks at regular intervals indicate a crystal-like structure (with triangular packing) around the centreline ($bin = 15$) for $e_n = 0.8$. It is clear that the origin of the crystal-like plug is tied to inelastic dissipation: 'dissipation-induced spatial-ordering'. Outside the plug region, ($bin = 1, 8$ in figure 30*b*), $g(x)$ is smooth, representing a gaseous structure.

The analogue of figure 30 for the densest flow $\nu = 0.85$ is shown in figure 31. Because the mean density is larger than the square packing density, a crystal-like structure is seen at the centre of the channel ($bin = 15$) even in the quasi-elastic limit (figure 31*a*), whereas a liquid-like structure persists in the shear layer $bin = 1, 5$. With increasing dissipation, the density correlations in the plug region are enhanced and the crystal structure in $bin = 15$ becomes nearly perfect, but the structure in the shear layer remains in the liquid regime (figure 31*b*).

5.2. *Spatial velocity correlation function*

The spatial velocity correlation functions are defined as (Pouliquen 2004; Baran *et al.* 2006)

$$C_{\alpha\beta}(x, y_k) \equiv C_{u_\alpha u_\beta}(x, y_k) = \frac{\left\langle \sum_{i=1}^{N} \sum_{j \geqslant i}^{N} u_\alpha^i u_\beta^j \delta(x - x_{ij}) \right\rangle}{\left\langle \sum_{i=j}^{N} u_\alpha^i u_\beta^j \right\rangle}, \tag{5.2}$$

where the subscripts α, β denote coordinate directions, superscripts i, j denote the particle number, $y = y_k$ is the bin location and the angular brackets indicate an average over time. When particle velocities are random the correlations are zero, so a non-zero value indicates correlated velocities.

The streamwise component of the spatial velocity correlation C_{xx} is shown in figures 32(*a*) and 32(*b*) for two mean densities, $\nu = 0.565$ and $\nu = 0.85$, respectively, with $e_n = 0.99$ and $\beta_w = 0.9$. For both densities, C_{xx} is close to zero in all bins; the

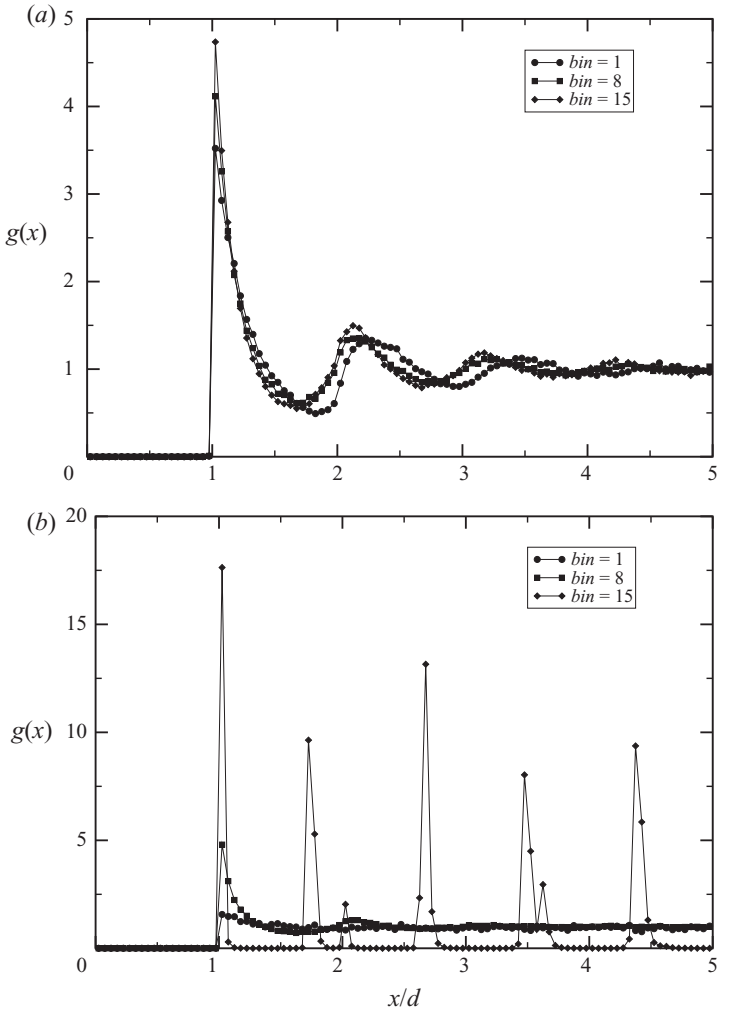

FIGURE 30. Pair correlation function, $g(x)$, in different bins at a density of $\nu = 0.565$ for smooth walls ($\beta_w = 0.9$), with (*a*) $e_n = 0.99$ and (*b*) $e_n = 0.8$. Total number of bins is 30.

other two components C_{yy} and C_{xy} are also close to zero (not shown). Despite having enhanced density correlation with increasing mean density (see figures 30*a* and 31*a* for $e_n = 0.99$), the spatial velocity correlations are found to be negligible at any location in the channel. It appears that the density correlations do not induce velocity correlations in the 'quasi-elastic' limit. That the velocity correlations are negligible at $\nu = 0.85$ justifies the use of Enskog's assumption even for a very dense granular system (Kumaran 2006).

Moving to a more dissipative case with $e_n = 0.8$, figures 33(*a*) and 33(*b*) display the variations of C_{xx} and C_{yy} for $\nu = 0.565$ and $\beta_w = 0.9$, respectively. Clearly, both velocity correlations are significantly enhanced in the plug region ($bin = 15$); the correlations decrease as we move away from the channel centreline and are negligible in the wall bin where the density is much smaller. Therefore, the enhancement of velocity correlations with increasing dissipation is closely tied to the local density: 'the larger the local density, the larger the amplification of velocity correlations is with increasing dissipation'.

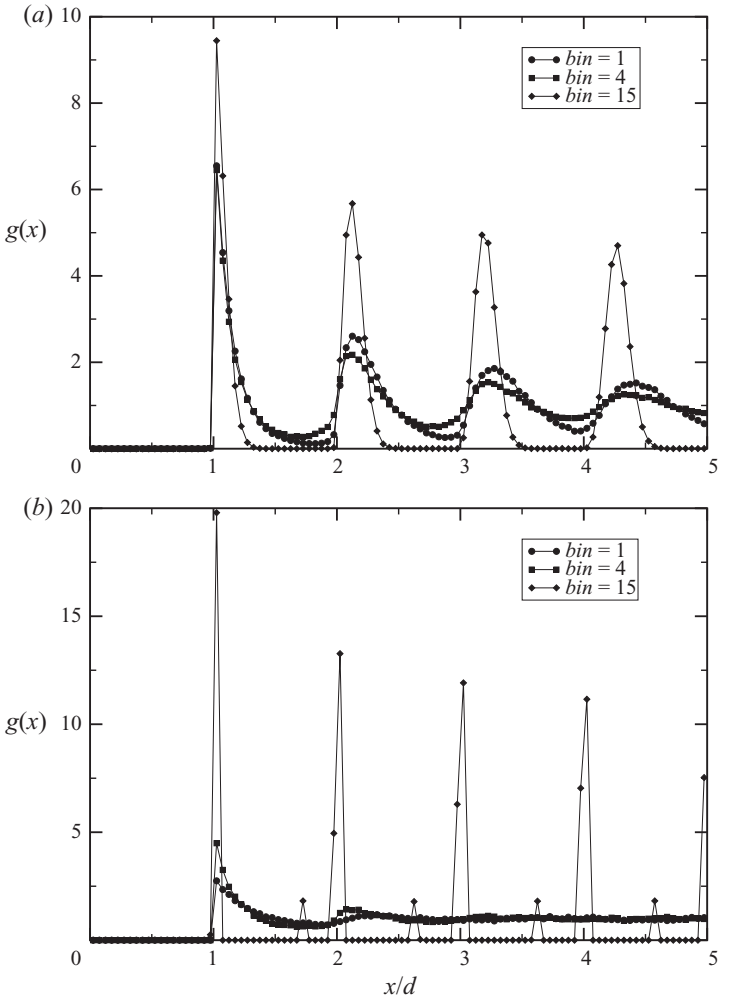

FIGURE 31. Same as figure 30, but for $\nu = 0.85$. Total number of bins is 30.

It is interesting to note that all three components of spatial velocity correlations become negative beyond a certain correlation length, $x/d \sim 8$ (see figure 33). This could be an indicator of circulatory-type motion for the fluctuating velocity field. To support this hypothesis of circulatory-type motion, the snapshots of the fluctuating velocity vectors of the particles in steady state are shown in figure 34. For clarity, the particles in a few bins (around the channel centreline) are shown. From these snapshots, it is clear that the velocity vectors of particles reverse after a certain length. This velocity-reversal phenomenon persists even at higher densities (similar to figure 34 and hence not shown). Therefore, the reversal of the fluctuating velocity field is responsible for the negative velocity correlation beyond some correlation length.

Three important points emerge from our study of correlation functions. First, our results confirm and support the previous findings (in different flow configurations) that inelastic collision indeed leads to enhanced velocity correlations (Blair & Kudrolli 2001; Prevost *et al.* 2002; Pouliquen 2004). Secondly, our study reveals that though density correlations (or spatial ordering of particles) play a significant role in

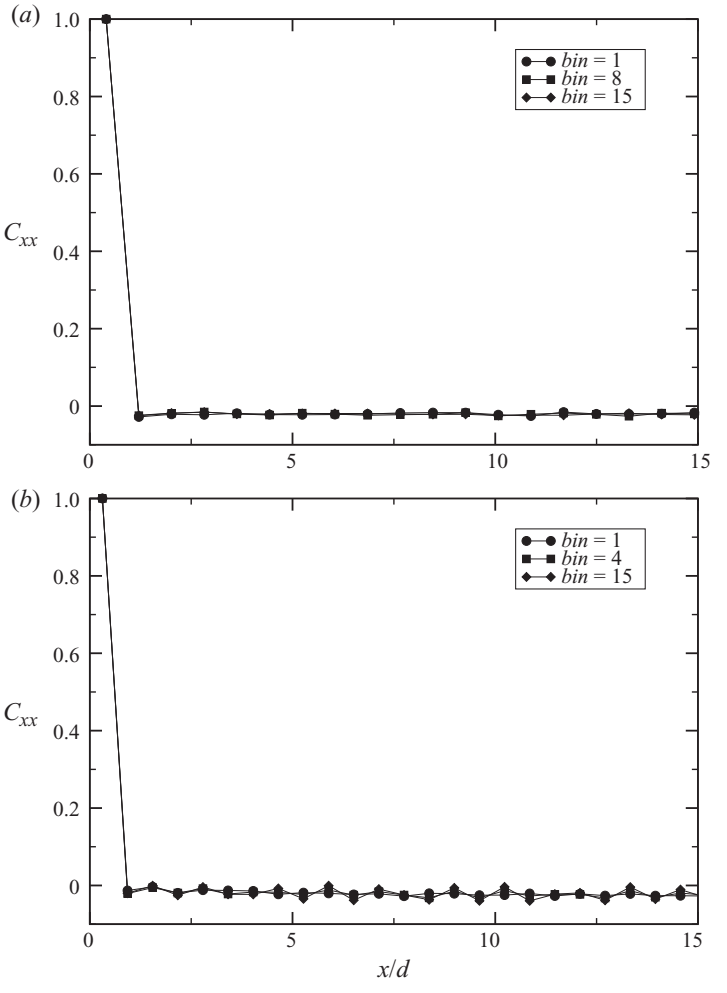

FIGURE 32. Streamwise velocity correlation function C_{xx} at (*a*) $\nu = 0.565$ and (*b*) $\nu = 0.85$ for quasi-elastic collisions $e_n = 0.99$ with smooth walls ($\beta_w = 0.9$). Total number of bins is 30.

enhancing the velocity correlations when the collisions are inelastic, however, they do not induce velocity correlations when the collisions are quasi-elastic, which is evident in figure 32. Thirdly, the latter point supports the use of Enskog's assumption of negligible velocity correlation for a very dense granular gas in the quasi-elastic limit. In view of the first two points, we therefore conclude that the enhanced density and velocity correlations around the channel centreline are responsible for the emergence of non-Gaussian velocity distributions with increasing dissipation.

6. Summary and conclusions

We have investigated the velocity distribution functions and the density and spatial velocity correlations in a gravity-driven Poiseuille flow of smooth inelastic hard disks using event-driven simulations in the rapid flow regime. Because the hydrodynamic fields are non-uniform across the wall-normal direction, a 'local' (binwise) study of distribution functions has been carried out with a detailed characterization of distributions via kurtosis and skewness. The effects of restitution coefficient (e_n), wall

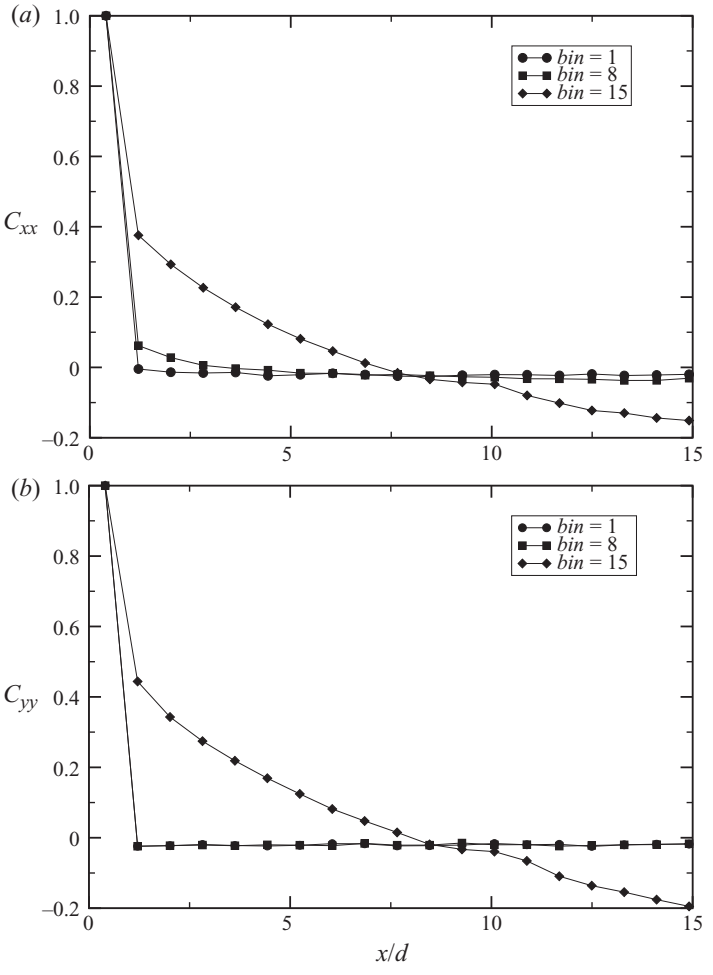

FIGURE 33. Variations of (*a*) C_{xx} and (*b*) C_{yy} in different bins for $e_n = 0.8$, $\nu = 0.565$ and $\beta_w = 0.9$. Total number of bins is 30.

roughness (β_w) and mean density (ν) on distribution functions and correlations have been studied. This is the first detailed simulation study on distribution functions and correlations in GPF, and our results are important to make a contact with the kinetic theory (Tij & Santos 2004) of granular materials for GPF.

The probability distributions of the fluctuating velocities in the x- and y-directions, denoted by $P(u_x)$ and $P(u_y)$, respectively, remain Gaussian in a quasi-elastic ($e_n \to 1$) granular Poiseuille flow with 'smooth' ($\beta_w \sim 1$) or 'perfectly rough' ($\beta_w \sim -1$) walls over a wide range of densities from dilute flows to much beyond the square-packing limit ($0.015 \leqslant \nu \leqslant 0.85$). The kurtosis of the distributions is found to be close to that of a Gaussian distribution in the quasi-elastic limit. Therefore, for GPF with smooth/perfectly rough walls, the Maxwellian/Gaussian is the leading-order velocity distribution function over a wide range of densities in the quasi-elastic limit. This is a surprising result for a dilute granular gas for which the Knudsen number belongs to the transitional flow ($0.1 < Kn < 10$) regime and, therefore, the higher-order effects due to large Kn are likely to be small in dilute GPF. The wall-roughness-induced dissipation ($\sim(1 - \beta_w^2)$ which is maximum at $\beta_w = 0$) can significantly affect the

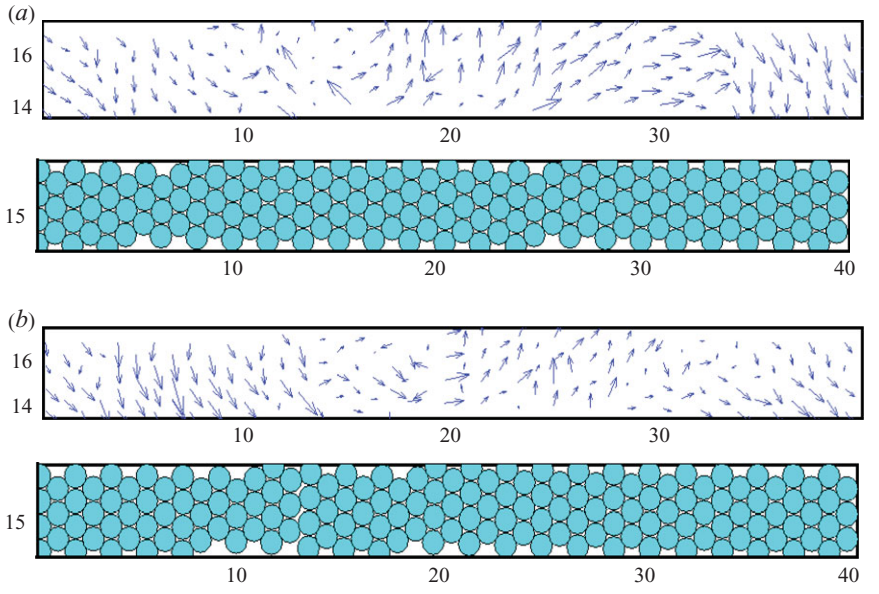

FIGURE 34. Snapshots of the fluctuating velocity vectors of the particles near the centreline of the channel at two different times (*a*) $t = 330$ and (*b*) $t = 340$ in the steady state for $\nu = 0.565$, $e_n = 0.8$ and $\beta_w = 0.9$. The numbers in the plots represent the coordinate values, and the flow is from left to right.

distribution functions that show up (i) in the distribution function for u_x in the form of a sharp peak for negative velocities (figure 13*a*) in the near-wall region and (ii) in the distribution function for u_y, which has a bimodal double-peak structure (figure 13*b*) for low velocities in the near-wall region. The above signature of wall roughness on $P(u_x)$ is felt at all points across the channel for dilute flows, as expected since $Kn \gg 1$ in the dilute limit, whereas for dense flows the velocity distributions only in the near-wall region are affected since $Kn \sim 0$ in the dense limit.

For moderately dense flows with smooth walls, the local velocity distributions become asymmetric with increasing dissipation, except near the walls where they remain Gaussian. Furthermore, the inhomogeneities due to the formation of density waves (a sinuous wave or a slug) are found to enhance the asymmetry of the velocity distributions. The signature of wall-roughness-induced dissipation, as mentioned above, persists even at larger dissipation.

At high densities ($\nu > 0.5$), an increase in inelastic dissipation is accompanied by the formation of a dense 'plug' (where the density approaches its maximum limit and the shear rate is negligibly small) around the channel centreline, surrounded by two shear layers (where the shear rate is high and the density is low) near the walls. The distribution functions within the shear layer follow the characteristics of those at moderate mean densities, with asymmetries that become stronger with increasing dissipation. The distribution functions near the walls remain close to a Gaussian for smooth walls even at larger dissipation. (A change in the wall roughness affects the distributions only in the near-wall region and the dynamics inside the shear layer as well as in the plug region remain relatively unaffected.) Within the plug, the high-velocity tails of both $P(u_x)$ and $P(u_y)$ distributions become overpopulated with increasing dissipation, and the tails seem to follow 'power-law' distributions (not very conclusive due to the limited range of data for high velocities) at higher dissipation. Comparing the tails of $P(u_x)$ and $P(u_y)$ distributions, we found that the streamwise

velocity fluctuations decay at a faster rate than its transverse component; this higher decay rate of u_x could be due to the stabilizing effect of gravity that is directed along the direction of u_x.

The degree of asymmetry of high-velocity tails, characterized in terms of the skewness of the respective distribution, increases with increasing inelastic dissipation. The skewness of $P(u_x)$ is negative in all the bins, whereas the skewness of $P(u_y)$ changes sign on either side of the channel centreline because of the underlying symmetry of the transverse velocity. The magnitude of the skewness of $P(u_x)$ and $P(u_y)$ is maximum in the shear layer where the shear rate is high and minimum in the plug region where the shear rate is negligible/small. The skewness of $P(u_x)$ is found to vary non-monotonically with mean density, with its maximum magnitude being located at $\nu \sim 0.3$. The emergence of density waves (and hence the related changes in the structure of the flow) seems to be responsible for the maximum skewness at $\nu \sim 0.3$; its magnitude decreases with increasing/decreasing density on either side of this critical density.

In the dense quasi-static regime of Poiseuille-type granular flow experiments (Moka & Nott 2005), the power-law tails of velocity distribution functions have been reported, and the experimental values for the exponents are of similar magnitude as in our simulations. However, in contrast to experimental findings that the distribution functions in the plug region (where the hydrodynamic gradients are negligible) are the same as in the shear layer (where gradients are sharp), our simulations show that the distribution functions in the plug region are markedly different from those in the shear layer. The sharp variation of density within the shear layer in our simulations could be responsible for the latter disagreement between simulation and experiment.

For dense flows, both the pair correlation function and the spatial velocity correlation functions have been probed to understand the origin of non-Gaussianity of the distribution functions. Within the plug region, the density and velocity correlations are enhanced with increasing inelastic dissipation. The flow outside the plug region is in a liquid state with negligible velocity correlations. At large enough dissipation, the spatial velocity correlations become negative beyond some correlation length, the origin of which has been shown to be tied to the sign reversal of the fluctuating velocity field beyond some distance. Our results confirm previous findings (Blair & Kudrolli 2001) that inelastic collision indeed leads to enhanced velocity correlations. Our work also reveals that the density correlations play a significant role in enhancing the velocity correlations when the collisions are sufficiently inelastic; however, they do not induce velocity correlations when the collisions are quasi-elastic for which the distribution functions are close to Gaussian. (This latter point provides some credence to the use of Enskog's assumption of negligible velocity correlation for a very dense granular gas in the quasi-elastic limit.) Therefore, the combined effects of enhanced density and velocity correlations around the channel centreline with increasing dissipation are likely to be responsible for the emergence of non-Gaussian velocity distributions in GPF.

M.A. acknowledges partial funding support from (i) the Department of Atomic Energy, Government of India (BARC/MA/4216) and (ii) the Max-Planck Partner Group at JNCASR (MPI/MA/4190) of MPIMM-Bremen, Max Planck Society, Germany. We thank all reviewers for helpful suggestions on the earlier version of this paper.

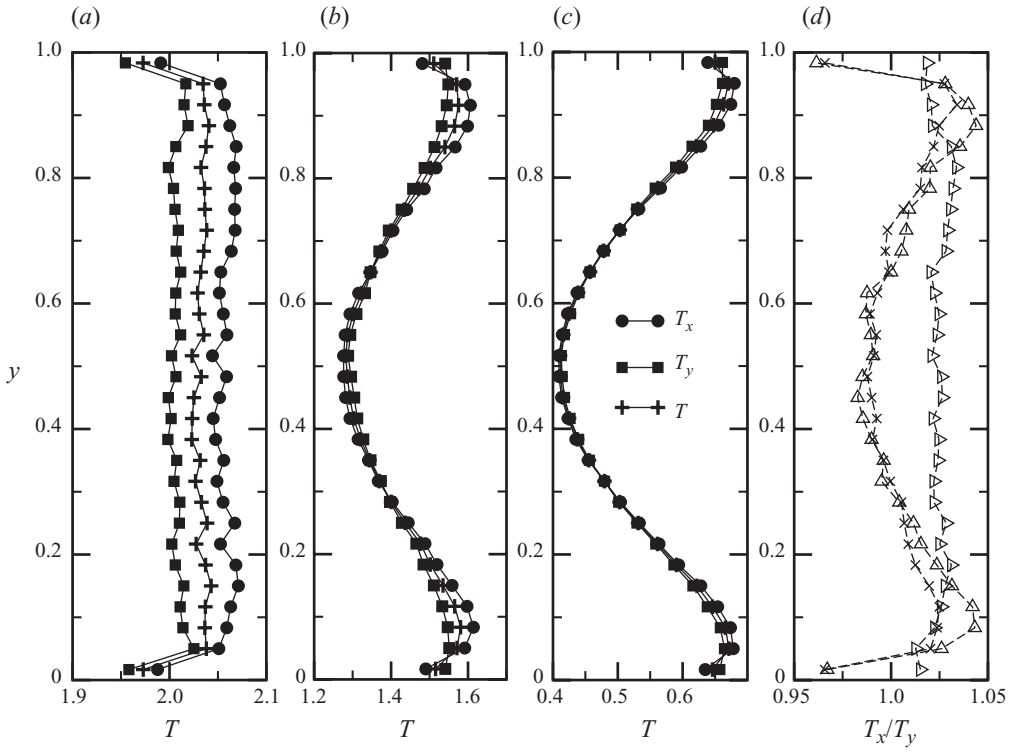

FIGURE 35. Variations of granular temperature (T, plus symbols) and its components (T_x, circles; T_y, squares) for smooth ($\beta_w = 0.9$) walls with quasi-elastic ($e_n = 0.99$) collisions: (*a*) $\nu = 0.015$; (*b*) $\nu = 0.294$; (*c*) $\nu = 0.565$; refer to figure 3 for other mean fields. (*d*) Variation of T_x/T_y with y for $\nu = 0.015$ (right triangles), 0.294 (up triangles) and 0.565 (crosses).

Appendix. Anisotropy of granular temperature

It is well known that the granular temperature is anisotropic (i.e. $T_x \neq T_y$, see (2.1*e*) and (2.1*f*) for definitions), which leads to normal stress differences (Sela & Goldhirsch 1998; Alam & Luding 2003, 2005). In fact, this anisotropic temperature is a signature of any driven system; for example, $T_x \neq T_y$ in a gravity-driven Poiseuille flow of elastic particles (Tij & Santos 2004) – the role of inelasticity is merely to amplify the degree of temperature anisotropy. In the following, we briefly discuss the temperature anisotropy in our simulations of GPF.

For parameter values of figure 3 ($\beta_w = 0.9$, smooth walls), we show the variations of T_x, T_y and T across the channel width in figure 35(*a–c*) at three mean densities ($\nu = 0.015$, 0.294 and 0.565), and the corresponding variation of temperature ratio (T_x/T_y) is shown in figure 35(*d*). It is seen from figure 35(*b*, *c*) that, similar to T, both T_x and T_y have bimodal shapes with temperature minima at the channel centreline for $\nu = 0.294$ and 0.565, but such bimodality of temperature profiles is not apparent for dilute flows ($\nu = 0.015$, figure 35*a*). For bimodal temperature profiles, the maxima of any temperature (T_x, T_y and T) shift towards the walls in the limit of perfectly smooth walls ($\beta_w \to 1$). It is clear from figure 35(*d*) that $T_x/T_y > 1$ in the dilute limit ($\nu = 0.015$); however, at moderate-to-dense flows $T_x/T_y < 1$ around the channel centreline (where a dense plug exists) and $T_x/T_y > 1$ on either side of the dense plug

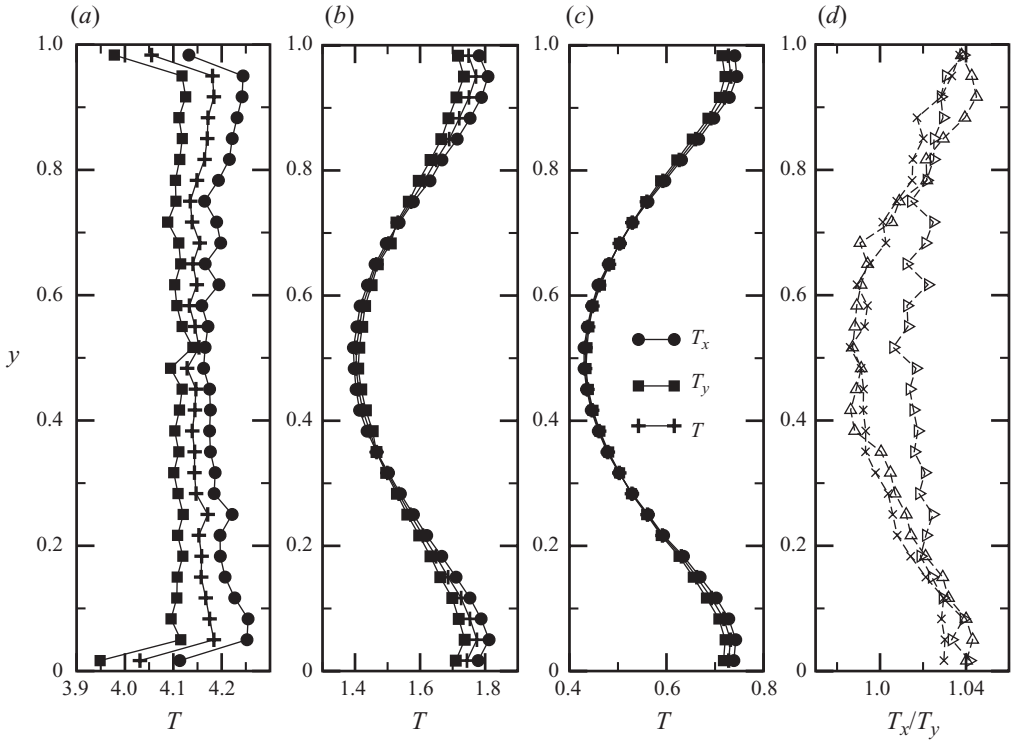

FIGURE 36. Same as figure 35, but for perfectly rough ($\beta_w = -1.0$) walls.

(except near the two walls). These overall features of temperature anisotropy also hold for perfectly rough ($\beta_w = -1$) walls as seen in figure 36(a–d).

Now we move to the case of rough ($\beta_w = 0.1$) walls for which the analogue of figure 35 is displayed in figure 37. One contrasting difference of temperature anisotropy for the rough wall case is that the bimodality of temperature (T_x, T_y and T) is clear even for dilute flows (see figure 37a); moreover, the temperature maxima at any density are more prominent for rough walls in comparison to smooth or perfectly rough walls. Regarding the temperature ratio for rough walls, $T_x/T_y < 1$ at any location in the dilute limit ($\nu = 0.015$), which is in variance ($T_x/T_y > 1$) with the smooth wall case; however, at moderate-to-dense flows the overall variations of $T_x/T_y < 1$ with y remain similar to the smooth wall case.

In general, it is expected that $T_x/T_y > 1$ in Posieuille flow of elastic particles (Tij & Santos 2004) because the particles are subject to a uniform acceleration along the x-direction. The principal signature of inelasticity is that T_x/T_y could be less than unity around the channel centreline at moderately dense to dense flows, irrespective of the wall roughness; this is presumably due to the collisional anisotropy within the dense plug as explained recently (Chikkadi & Alam 2009) in terms of the 'sign-change' of the first normal stress difference. One interesting finding of the present paper is that in the dilute limit $T_x/T_y < 1$ at any location when the walls are made rough ($\beta_w \sim 0$), which can be explained by analysing the wall model in our simulations. Following our wall model (see § 2.1), the tangential component of particle velocity is changed ($c'_x = \beta_w c_x$) upon a particle–wall collision but its normal component ($c'_y = -e_w c_y$) remains unchanged since $e_w = 1$ in the present simulations. Therefore, the streamwise temperature ($T_x \sim \langle c'^2_x \rangle$) is expected to be lower than its transverse

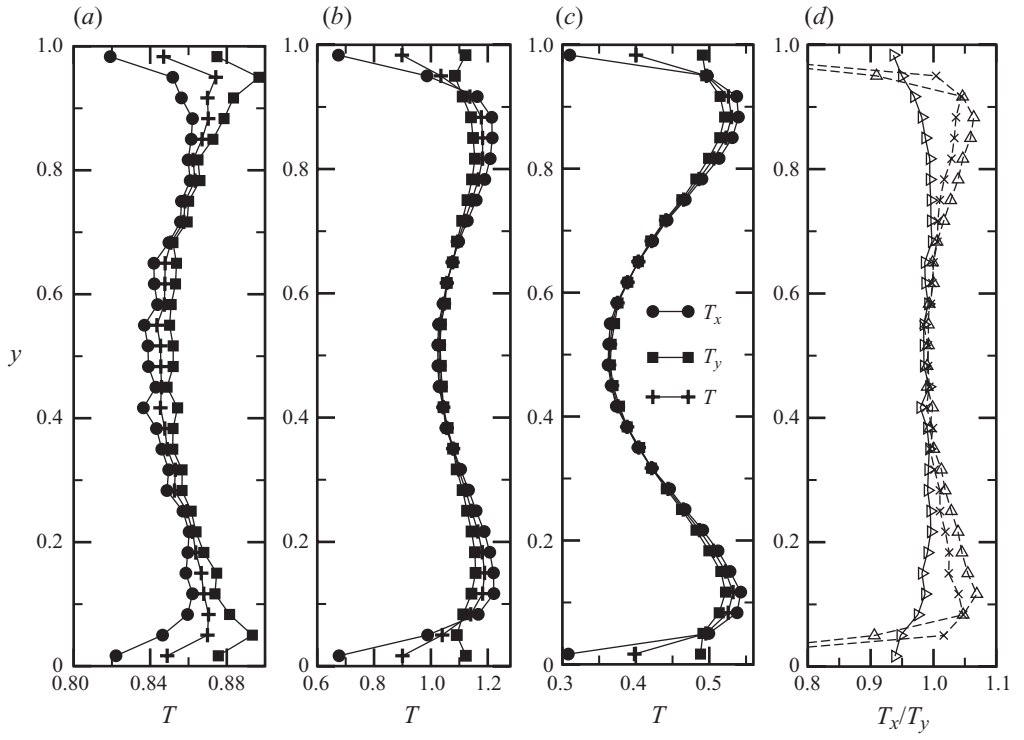

FIGURE 37. Same as figure 35, but for rough ($\beta_w = 0.1$) walls.

component ($T_y \sim \langle c_y'^2 \rangle$) when $\beta_w \sim 0$, leading to $T_x/T_y < 1$ near the walls. In the dilute limit, we recall that the Knudsen number is of order unity or larger in the present simulations, and hence the dynamics (and temperature) are largely determined by particle–wall collisions, resulting in $T_x/T_y < 1$ at any location for $\nu = 0.015$ (see the line with circles in figure 37*d*).

Because the granular temperature ratio is directly tied to normal stress differences, the first normal stress difference ($\mathscr{N}_1$) is likely to reverse its sign across the channel width for moderately dense to dense GPF for any wall roughness; in the dilute limit, $\mathscr{N}_1$ remains positive/negative at any location for smooth/rough walls, respectively. For related issues on the first normal stress difference and its sign reversal in GPF, the readers are referred to our recent paper (Chikkadi & Alam 2009).

Recall that the dissipation due to wall–particle collisions ($\sim(1 - \beta_w^2)$) is maximum for rough walls ($\beta_w \sim 0$) and vanishes in the limiting cases of smooth ($\beta_w \to 1$) and perfectly rough ($\beta_w = -1$) walls. All the above observations support our conclusion that the bimodality of granular temperatures and their ratios in our simulations of GPF are primarily controlled by the wall-roughness-induced dissipation.

REFERENCES

ALAM, M., CHIKKADI, V. & GUPTA, V. K. 2010 Density waves and the effect of wall roughness in granular Poiseuille flow: simulation and linear stability. *Eur. Phys. J. ST* (in press).

ALAM, M. & LUDING, S. 2003 First normal stress difference and crystallization in a dense sheared granular fluid. *Phys. Fluids* **15**, 2298.

ALAM, M. & LUDING, S. 2005 Energy noequipartition, rheology and microstructure in sheared bidisperse granular mixtures. *Phys. Fluids* **17**, 063303.

Alam, M., Willits, J. T., Aranson, B. Ö. & Luding, S. 2002 Kinetic theory of a binary mixture of nearly elastic disks with size and mass disparity. *Phys. Fluids* **1**4, 4085.

Aranson, I. & Tsimring, L. S. 2006 Patterns and collective behaviour in granular media: theoretical concepts. *Rev. Mod. Phys.* **78**, 1641.

Baran, O., Ertas, D., Halsey, T. C., Grest, G. S. & Lechman, J. B. 2006 Velocity correlations in dense gravity-driven granular chute flow. *Phys. Rev.* E **74**, 051302.

Baxter, G. W. & Olafsen, J. S. 2003 Kinetics: Gaussian statistics in granular gases. *Nature* **425**, 680.

Blair, D. & Kudrolli, A. 2001 Velocity correlations in dense granular gases. *Phys. Rev.* E **64**, 050301.

Brey, J. J., Dufty, J. W. & Santos, A. 1999 Kinetic models for granular flow. *J. Stat. Phys.* **97**, 281.

Brilliantov, N. & Pöschel, T. 2004 *Kinetic Theory of Granular Gases.* Oxford University Press.

Campbell, C. S. 1990 Rapid granular flows. *Annu. Rev. Fluid Mech.* **22**, 57.

Cafiero, R., Luding, S. & Herrmann, H. J. 2000 Two-dimensional granular gas of inelastic spheres with multiplicative driving. *Phys. Rev. Lett.* **84**, 6014.

Chikkadi, V. & Alam, M. 2009 Slip velocity and stresses in granular Poiseuille flow via event-driven simulation. *Phys. Rev.* E **80**, 021303.

Esipov, S. & Pöschel, T. 1997 The granular phase diagram. *J. Stat. Phys.* **86**, 1385.

Garzo, V. & Dufty, J. W. 1999 Dense fluid transport for inelastic hard spheres. *Phys. Rev.* E **59**, 5895.

Gayen, B. & Alam, M. 2008 Orientation correlation and distribution functions in uniform shear flow of a dilute granular gas. *Phys. Rev. Lett.* **1**00, 068002.

Goldhirsch, I. 2003 Rapid granular flows. *Annu. Rev. Fluid Mech.* **35**, 267.

Goldhirsch, I. & Tan, M.-L. 1996 The single particle distribution function for rapid granular shear flows of smooth inelastic disks. *Phys. Fluids* **8**, 1752.

Haff, P. K. 1983 Grain flow as a fluid-mechanical phenomenon. *J. Fluid Mech.* **134**, 401.

Herrmann, H. J. & Luding, S. 1998 Modeling granular media on the computer. *Continuum Mech. Therm.* **10**, 188.

Hui, K., Haff, P. K., Ungar, J. E. & Jackson, R. 1984 Boundary conditions for high-shear grain flows. *J. Fluid Mech.* **145**, 223.

Jenkins, J. T. & Richman, M. W. 1986 Boundary conditions for plane flows of smooth, nearly elastic, circular disks. *J. Fluid Mech.* **171**, 53.

Jenkins, J. T. & Savage, S. B. 1983 A theory for the rapid flow of identical, smooth, nearly elastic, spherical particles. *J. Fluid Mech.* **130**, 187.

Karniadakis, G. & Beshok, A. 2001 *Micro Flows: Fundamentals and Simulation.* Springer.

Kumaran, V. 2006 Granular flow of rough particles in the high-Knudsen-number limit. *J. Fluid Mech.* **561**, 43.

Liss, E., Conway, S. L. & Glasser, B. J. 2002 Density waves in gravity-driven granular flow through a channel. *Phys. Fluids* **14**, 3309.

Losert, W., Cooper, D., Delour, J., Kudrolli, A. & Gollub, J. P. 1999 Velocity statistics in vibrated granular media. *Chaos* **9**, 682.

Lubachevsky, B. 1991 How to simulate billiards and similar systems. *J. Comp. Phys.* **94**, 255.

Lun, C. K. K. 1991 Kinetic theory for granular flow of dense, slightly inelastic, slightly rough spheres. *J. Fluid Mech.* **233**, 539.

Mitarai, N., Hayakawa, H. & Nakanishi, H. 2002 Collisional granular flow as a micropolar fluid. *Phys. Rev. Lett.* **88**, 174301.

Moka, S. & Nott, P. R. 2005 Statistics of particle velocities in dense granular flows. *Phys. Rev. Lett.* **95**, 068003.

Montanero, J. M. & Santos, A. 2000 Computer simulation of uniformly heated granular fluids. *Gran. Matter* **2**, 53.

Moon, S. J., Shattuck, M. D. & Swift, J. B. 2001 Velocity distributions and correlations in homogeneously heated granular media. *Phys. Rev.* E **64**, 031303.

Natarajan, V. V. R., Hunt, M. L. & Taylor, E. D. 1995 Local measurements of velocity fluctuations and diffusion coefficients for a granular material flow. *J. Fluid Mech.* **304**, 1.

van Noije, T. P. C. & Ernst, M. H. 1998 Velocity distributions in homogeneous granular fluids: the free and the heated case. *Gran. Matter* **1**, 52.

Pouliquen, O. 2004 Velocity correlations in dense granular flows. *Phys. Rev. Lett.* **93**, 248001.

Prevost, A., Egolf, D. A. & Urbach, J. S. 2002 Forcing and velocity correlations in a vibrated granular monolayer. *Phys. Rev. Lett.* **89**, 084301.

Puglisi, A., Loreto, V., Marconi, U., Petri, A. & Vulpiani, A. 1998 Clustering and non-Gaussian behaviour in granular matter. *Phys. Rev. Lett.* **81**, 3848.

Rouyer, F. & Menon, N. 2000 Velocity fluctuations in a homogeneous 2D granular gas in steady state. *Phys. Rev. Lett.* **85**, 3676.

Sela, N. & Goldhirsch, I. 1998 Hydrodynamic equations for rapid shear flows of smooth, inelastic spheres, to Burnett order. *J. Fluid Mech.* **361**, 41.

Taguchi, Y. & Takayasu, H. 1995 Power-law velocity fluctuations due to inelastic collisions in numerically simulated vibrated bed of powder. *Europhys. Lett.* **30**, 499.

Tij, M. & Santos, A. 2004 Poiseuille flow in a heated granular gas. *J. Stat. Phys.* **117**, 901.

Vijayakumar, K. C. & Alam, M. 2007 Velocity distribution and the effect of wall roughness in granular Poiseuille flow. *Phys. Rev.* E **75**, 051306.

van Zon, J. S. & MacKintosh, F. C. 2004 Velocity distributions in dissipative granular gases. *Phys. Rev. Lett.* **93**, 038001.